Machine learning-aided estimation of minimum pressure from sparse velocity data in vortex flows

Xianzhang Xu, Daria Skalitzky, and Krishnan Mahesh
Center for Naval Research and Education and University of Michigan, Ann Arbor, Michigan, USA

(Received 25 November 2025; accepted 6 May 2026; published 26 May 2026)

We apply a physics-informed deep learning method to reconstruct the flow field from sparse and noisy particle tracks, focusing on accurately assimilating the global minimum pressure on a fine-grid domain from very sparse velocity data. The spatial resolution of the velocity data could be much larger than the mesh spacing of the reconstructed flow field. To address this problem, we first quantify the performance of the physics-informed neural network (PINN) model using a series of analytical vortex models. Synthetic particle data are generated using the analytical solutions of the velocities; the PINN model is trained on these sparse particle measurements, and the model then reconstructs the finer-resolution flow field within a fixed domain of interest and obtains the minimum pressure. We also investigate the effects of the reconstruction resolution, particle densities, particle distributions, incomplete measurements, velocity noise, and noise in spatial coordinates. The methodology is applied to a turbulent flow of interacting counterrotating vortices of unequal strength obtained from Large-Eddy Simulation, and the results are discussed.

DOI: 10.1103/3hbh-przx

I. INTRODUCTION

Obtaining the pressure field in flows is important to a variety of applications. For example, cavitation inception, defined as the initial rapid growth of bubbles, occurs when the minimum pressure in the fluid drops below vapor pressure [1]. It is important to know the operating conditions at which these incepting pressures are attained. These low pressures typically occur in highly localized, small-scale, strained vortices that are both spatially and temporally intermittent. Particle image velocimetry (PIV) and particle tracking velocimetry (PTV) are widely used in experiments to measure the flow velocities [2]. However, the pressure fields are not directly measured and must be inferred from the particle measurements. Furthermore, the minimum pressure can be difficult to accurately measure due to the sparse distribution of particles around vortex cores as observed in [3]. These challenges motivate the current work. Figure 1 shows a schematic overview of our problem. Consider a complex turbulent flow, such as the flow in the tip gap of a ducted propulsor from the simulations of [4]. Note the dominance of small-scale co- and counterrotating vortices whose interaction significantly influences the minimum pressures. We imagine a volume of interrogation illustrated by the box where Lagrangian measurements from particles are obtained. The measurements are assumed sparse, due to particles being flung out of the cores of small vortices, and noisy due to inherent experimental uncertainties. We attempt to obtain the minimum pressure by reconstructing the velocity and pressure fields on a fine Eulerian grid. We first emulate this scenario by generating sparse and noisy measurements of velocities for certain canonical vortex flows, and then apply the methodology to a complex turbulent flow.

Flow field reconstruction, especially the pressure field, is challenging. One of the most common approaches isolates the pressure gradient terms from the incompressible Navier-Stokes equations and solves the Poisson equation for pressure [5]. Similarly, some works directly integrate the pressure gradient from the Navier-Stokes equation along a specific path in the flow field [6]. The

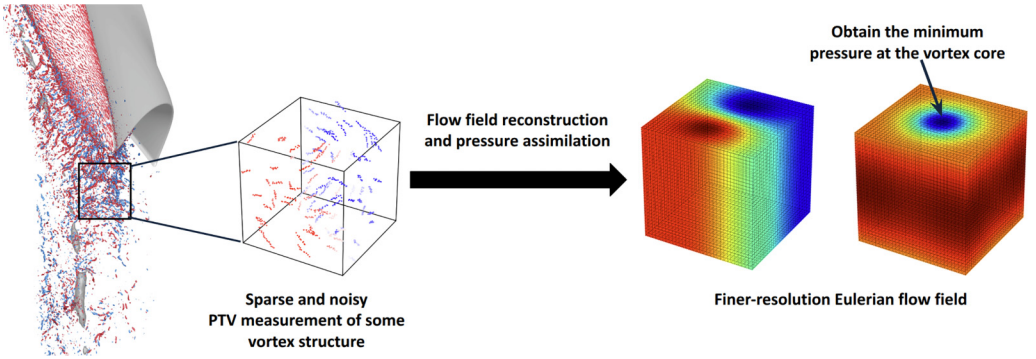

FIG. 1. Conceptual map of the flow field reconstruction problem for vortex flow. The figure on the far left is from the simulations of [4].

work in [7] introduced a virtual boundary integration scheme to obtain the pressure distribution by integrating the material acceleration. Another approach considers the flow field reconstruction as a data assimilation problem. For example, the work in [8] showed a PTV-DNS hybrid simulation using the Kalman filter to assimilate the velocity and pressure fields from sparse PTV data at Re $\approx$ 2000. The work in [9] used a generalized least squares method to incorporate the uncertainty of the pressure gradient into the optimization process to reconstruct the pressure field. Some works [10,11] use ensemble-based and adjoint-based variational methods. Recently, machine learning methods have attracted much attention in solving fluid dynamics problems. In [12] a convolutional neural network (CNN) is used to infer the solution of the 2D Poisson equation on a Cartesian grid. Physics-informed Neural Networks (PINNs) [13], which are a type of deep learning model that incorporates the physical governing equations into the training loss function of the neural network, have been used in related problems. References [14] and [15] have implemented PINNs to improve the accuracy of PIV measurements and PTV reconstructions, and also to assimilate the pressure field of turbulent flow, as shown in [16]. However, these previous works lack a systematic study on the flow reconstruction results, especially for the minimum pressure in the flow field. Additionally, the performance of PINNs under different average distances between the sampled data and the reconstruction mesh sizes is not fully considered. The sensitivity of PINNs to certain measurement factors, such as particle density, noise source, and levels, also requires further quantification. Figure 2 shows the example of the average distance of the sampled data points and the mesh grid size

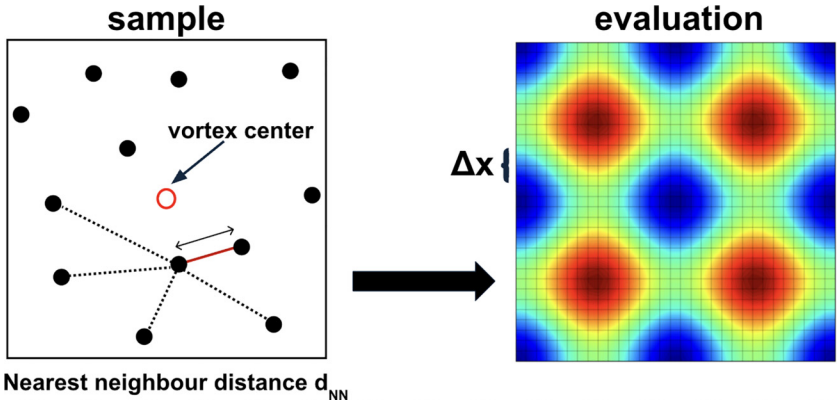

FIG. 2. Illustration of the resolution of sampled data and reconstruction flow field.

of the reconstruction flow field; the details of these two distances are introduced in Sec. II C. This work focuses on a systematic study of the application of the PINN model for the specific objectives, i.e., reconstructing a finer flow field from sparse and noisy velocity data points and assimilating the minimum pressure.

We seek a comprehensive study of the performance of PINNs for these tasks. We apply a framework based on PINNs to reconstruct the flow field, assimilate the pressure field, and obtain the global minimum pressure. A convergence study for the minimum pressure in spatial resolution and temporal history is also conducted. This work also provides a sensitivity analysis of the PINN model to the density of measurement points, as well as the measurement noise in velocity and the errors in spatial coordinates. A series of canonical vortex models in two and three dimensions is used as the benchmark to study the performance of the PINN model towards the goal. Synthetic velocity measurement data are generated using the analytical solutions of the vortex models, which are also used to generate the fine flow fields of both the velocity and the pressure for validation and testing. Further investigations are performed to test the effects of different particle distributions and noise levels. The paper is organized as follows: Sec. II introduces the fundamental background of the deep learning model and presents the canonical vortex models. The entire framework is summarized. Section III shows the flow field reconstruction results from the synthetic data. Section IV discusses how particle densities and the different noise sources can affect the accuracy and the uncertainty of the flow field reconstruction. Section V shows the implementation of the same framework on a twin vortex problem obtained from high-fidelity numerical simulations. A brief summary in Sec. VI concludes the paper.

II. METHODOLOGY

This section reviews the technical details of the deep learning model used in this work, Physics-informed Neural Networks. It also introduces the analytical vortex flow models in both two and three dimensions, with analytical expressions that are used to generate the training and verification data. Finally, the framework designed to emulate sparse particle measurement data with velocity information, reconstruct the entire flow field, and estimate the pressure field of interest is introduced.

A. Physics-informed neural networks

Physics-informed Neural Networks (PINNs) were originally introduced to train the deep-learning model to learn the complex physical systems governed by the partial differential equations (PDEs), which are usually difficult to learn using regular neural networks [13]. PINNs are based on a multilayer perceptron (MLP) neural network architecture, which contains an input layer, multiple hidden layers, and an output layer. The inputs of PINNs are usually some data points of spatial and temporal coordinates based on the dimension of problems, and the outputs of PINNs are some physical variables of interest such as velocity, temperature, forces, and pressure. A main feature that distinguishes PINNs from regular MLP neural networks is the loss function. Since many complex physical systems are governed by time-dependent PDEs that require the computation of derivatives of key features with respect to the spatial and temporal variables, PINNs incorporate these PDEs into the loss function that is used to train the neural networks. These data points are sampled to compute the data loss, similar to regular MLP neural networks. With partially observed data points in velocity, it is not necessary to specify additional boundary conditions and initial conditions, then add them to the total loss functions. The total loss function used in this work can be expressed as

$$L = \lambda_d L_d + \lambda_p L_p. \tag{1}$$

Here λ_d is the weight coefficient corresponding to the loss of data, and L_p is the loss of physical equations (PDEs). For the fluid problem, it is natural to take the Navier-Stokes equations as the physical loss equation, and the velocities and the pressure as the outputs when the external forces are negligible. In this work, specifically, the data loss is computed as the mean squared error (MSE)

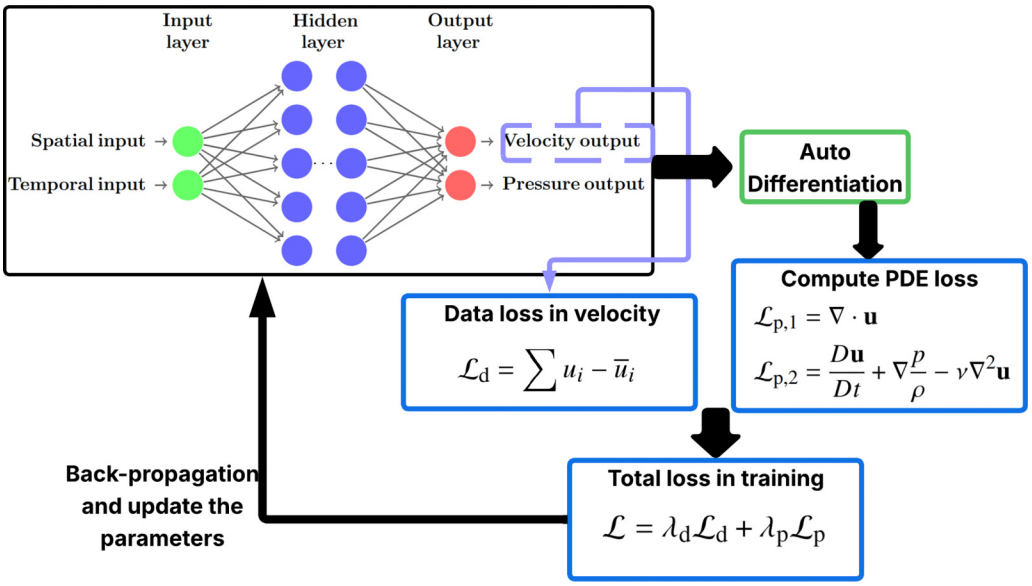

FIG. 3. The architecture of PINNs with incompressible Navier-Stokes equations.

between the outputs from the PINN model and the sampled particle data, while the physical loss is computed as the residual of the incompressible Navier-Stokes equation

$$\mathcal{L}_d = \sum_{i=1}^{N_s} \frac{1}{N_s}(\boldsymbol{u}_i - \overline{\boldsymbol{u}}_i)^2 \quad \text{and} \quad \mathcal{L}_{p,1} = \sum_{i=1}^{N_s} \frac{1}{N_f}\nabla \cdot \mathbf{u}, \quad \mathcal{L}_{p,2} = \sum_{i=1}^{N_f} \frac{1}{N_s}\left(\frac{D\boldsymbol{u}_i}{Dt} + \nabla\frac{p_i}{\rho} - \nu\nabla^2\mathbf{u}_i\right)^2. \tag{2}$$

Here N_s stands for the total number of sampled points from the particle data, and N_f is the total number of collocation points that are randomly sampled inside the computational domain to compute the physical residuals based on the PDEs. $\boldsymbol{u}$ and $\overline{\boldsymbol{u}}$ are the velocity sampled from the particles and the velocity computed by the neural network, respectively. The pressure is unknown from the training data and will be assimilated from the neural network by minimizing the residual of the physical equations. In some works [16,17], the total loss also includes the loss computed from initial and boundary conditions. However, those can also be considered as part of the data loss, and they are not considered in this work since the particle data have been included in the data loss term. Each term in Eq. (1) can be independent of the others, which means that the sample points used to calculate the data loss are not necessarily the same as the points used to calculate the PDE loss or the boundary loss. This makes PINNs flexible in terms of the data required to train the neural networks, where the regular neural networks often require sufficient good-quality data. When no training data are available, the loss function of PINNs becomes the objective of solving a PDE with specific boundary conditions. When some training data are available, PINNs can be trained with those sample data and the PDE loss of the collocation points to assimilate the unknown variables in the output layer.

Figure 3 summarizes the architecture of PINNs when the incompressible Navier-Stokes equations are used as the physics information. Here the inputs are the spatial coordinates $\boldsymbol{x}$ and the temporal coordinates t, and the outputs are the velocities $\boldsymbol{u}$ and pressure p corresponding to the inputs $(\boldsymbol{x}, t)$. The outputs are postprocessed by computing their derivatives with respect to the spatial and temporal inputs and substituting them into the momentum equations and the continuity equation to satisfy the incompressibility condition. The parameters of the neural networks are

updated by backpropagation to ensure that the gradient of the total loss function keeps decreasing through iterations. Using the autodifferentiation method, the gradient can be quickly computed in a Python library such as PyTorch [18].

B. Analytical vortex models

We use three analytical vortex models in both two and three dimensions as benchmarks for flow field and minimum pressure reconstruction. These vortex models with analytical solutions can be used to generate both the synthetic Lagrangian particle measurements for training and also the fine-resolution Eulerian flow field data for validation. Here we briefly introduce all the vortex models.

1. Taylor-Green vortex

The Taylor-Green vortex is a time-dependent analytical solution to the incompressible Navier-Stokes equations. The velocity field in Cartesian coordinates of the 2D Taylor-Green vortex is given as

$$u(x, y, t) = -U\cos(x)\sin(y)e^{-2\nu t} \text{ and } v(x, y, t) = U\sin(x)\cos(y)e^{-2\nu t}, \tag{3}$$

where U is a characteristic velocity and ν is the kinematic viscosity. The pressure field can also be derived from the velocity field expression in Eq. (3),

$$p(x, y, t) = p_0 - \frac{\rho U^2}{4}[\cos(2x) + \cos(2y)]e^{-4\nu t}, \tag{4}$$

where ρ is the density of the fluid and p_0 is a reference pressure.

2. Lamb-Oseen vortex

The Lamb-Oseen vortex is a solution to the Navier-Stokes equations that describes the diffusion of an initially concentrated axisymmetric vortex in a viscous fluid. The velocity field of the Lamb-Oseen vortex is given in cylindrical coordinates:

$$v_r = 0, \quad v_\theta(r, t) = \frac{\Gamma}{2\pi r}\left(1 - e^{-r^2/(4\nu t)}\right), \quad v_z = 0, \tag{5}$$

where ν is the kinematic viscosity and Γ is the initial circulation. The pressure field can be obtained by integrating the radial momentum equation:

$$\frac{\partial p}{\partial r} = \rho\frac{v_\theta^2}{r}, \tag{6}$$

where v_θ is the azimuthal velocity and ρ is the density of the fluid. Lamb-Oseen vortex flow models the structure of real vortices that have a small core surrounded by a nearly inviscid region, and it incorporates unsteadiness through viscous diffusion. The Lamb-Oseen vortex model is selected as the canonical vortex flow to help understand how the distribution and density of the particles affect the flow reconstruction results in Sec. IV A.

3. Burgers' vortex

Burgers' vortex is an exact solution to the Navier-Stokes equations in three dimensions. Burgers' vortex model describes a steady axisymmetric vortex in a viscous fluid and is subjected to a constant axial stretching rate $a > 0$. Since the stretching balances viscous diffusion, the vortex is in a steady state. The velocity field of the Burgers' vortex in cylindrical coordinates is given as

$$v_r = -ar, \quad v_\theta(r) = \frac{\Gamma}{2\pi r}\left(1 - e^{-ar^2/(2\nu)}\right), \quad v_z = 2az, \tag{7}$$

where ν is the kinematic viscosity and Γ is the circulation. Similar to the Lamb-Oseen vortex, the pressure field can be obtained by integrating

$$\frac{\partial p}{\partial r} = -a^2 r + \frac{v_\theta^2}{r}. \tag{8}$$

C. Flow field reconstruction framework

The data generation procedure generates the synthetic sparse particle data in Lagrangian coordinates for training, and also the fine resolution Eulerian flow field data for validation and testing. The input variables of the PINN model are the spatial coordinates and the time steps, and the output variables are the velocities and the pressure. In the training procedure, the sparse particle data, which include $(\boldsymbol{x}, t)$ and velocities $\boldsymbol{u}$, are given to the PINN model, which uses the sparse velocity data to learn the maps between the spatial-temporal coordinates and the flow field quantities along with the given physical information, i.e., the incompressible Navier-Stokes equations. In addition to the particle data, the training samples also collect random points inside the domain of interest where no velocity information is available. These points are used to compute the physical loss only. In some PINN works, the sample points also contain the points at boundaries and initial time, but they are not necessary for this work since the particle data have already provided the data loss contribution as shown in Eq. (1). The training procedure ends when the training loss converges or reaches the predefined maximum iterations. Then the trained model is evaluated at a fine resolution of the spatial coordinates, where the validation loss for both the velocities and the pressure is computed using the MSE. In this work, the spatial grid sizes are different between the training and testing procedures since they are generated from two different approaches. The time step sizes are the same, but they could be different as desired by the problem of interest. In addition, the velocities and pressure on the fine coordinates predicted by the PINN model are compared with the pregenerated validation data, and the $\mathcal{L}_2$ relative errors for each variable are calculated.

In Fig. 2 the sample and evaluation distance between data points are shown, where for the sample data points we calculate the nearest-neighbor distance d_{nn}, the mean of the distances from each randomly generated point to its closest other point. The distance between the evaluation grid sizes is straightforward, since the evaluation flow field is in a fixed size. These two distances are nondimensionalized by the maximum radius of the vortex r_m,

$$d_{nn}^* = \frac{d_{nn}}{r_m} \quad \text{and} \quad \Delta x^* = \frac{\Delta x}{r_m}. \tag{9}$$

For example, when the particle density is 10×10, $d_{nn}^* = 0.177$ for the Lamb-Oseen vortex, and the evaluation resolution 64×64 gives $\Delta x^* = 0.044$.

Figure 4 summarizes the entire framework using the Burgers' vortex flow as an example. The details of the data generation process for each vortex model are introduced in Sec. III A. For the turbulent twin vortex flow, the training data are down-sampled from a high-fidelity LES simulation, and the original dataset is used for validation. More details will be presented in Sec. V. For all the canonical vortex flows, the PINN model is adapted from an open-source library DeepXDE [19]. Besides the sparse data points, a total of 10 000 random collocation points are added for each individual case to compute the physical loss only. These collocation points are set to be fixed for the entire training procedure. The training is manually scheduled with a reducing learning rate from 1×10^{-3} to 1×10^{-5}, and the optimizers are "Adam" [20]. To avoid overfitting, we employed an early-stopping criterion by validating the model after 10 000 steps, and the training will stop when the $\mathcal{L}_2$ relative error of the predicted pressure field is less than 5%. For consistency, all three analytical vortex flows use eight-layer neural networks with 100 neurons per layer. The activation function is the hyperbolic function, tanh. The weights of the data loss and physical loss are set to be equal, i.e., 1 for both λ_d and λ_p for all the training steps. The simulations are performed on a single NVIDIA A100 GPU.

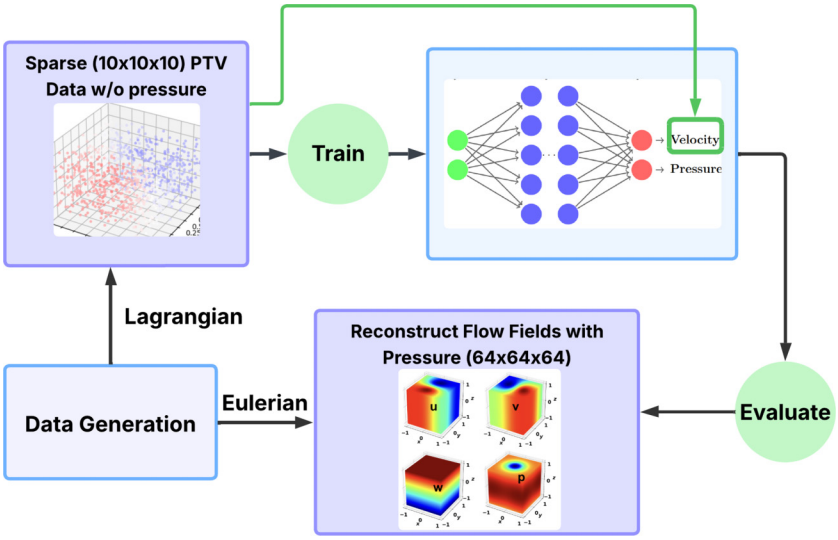

FIG. 4. Flow field reconstruction framework using PINNs.

III. SYNTHETIC PARTICLE DATA GENERATION AND FLOW FIELD RECONSTRUCTION RESULTS

The data generation process for training and validation is introduced. Also, the flow field reconstruction results for the three vortex models are discussed.

A. Data generation

We aim to emulate the situation when the particles are sparse and may be localized away from the low-pressure core. The analytical solution of the vortex models can be used to generate synthetic particle tracks for training. Particle data collect velocity information using the Lagrangian method, in which the motion of individual tracer particles is tracked across successive image frames to reconstruct their trajectories. Therefore, the synthetic particle data are initially generated by a low density, such as 10×10, where each dimension has the corresponding number of random coordinates and results in a total of 100 points. After that, at each time step, every single particle moves one time step forward based on

$$x_{k+1} = x_k + \int u_k d\tau, \quad y_{k+1} = y_k + \int v_k d\tau. \tag{10}$$

Here 21 time steps are sampled to generate the training data.

Figure 5 shows an example of the particles generated for Taylor-Green vortex with a density of 10×10 in a domain of $[-\pi, \pi]$, with $U = 1$, and $\nu = 0.01$. Figure 5(a) shows the initial distribution of the particles and the corresponding velocities, and Fig. 5(b) shows the entire trajectories with the color map indicating the v velocity. The time window is from 0.1 to 2, with a total of 21 time steps. It is clear that the particle trajectories align well with the analytical solution of the Taylor-Green vortex. Note that the particles are not set to be periodic, so that some particles could move outside the domain of interest. The figure only shows the particles inside the domain. The pressure data are set to be unknown during training, since they are rarely available from particle measurements, and the objective of this work is to assimilate the pressure field from sparse particle tracks.

Similar to the Taylor-Green vortex flow, the training data for the Lamb-Oseen vortex flow are generated by initially sampling 10×10 random points and tracking their positions using the analytical solution of the velocities. Figure 6 shows the particle distribution of the Lamb-Oseen

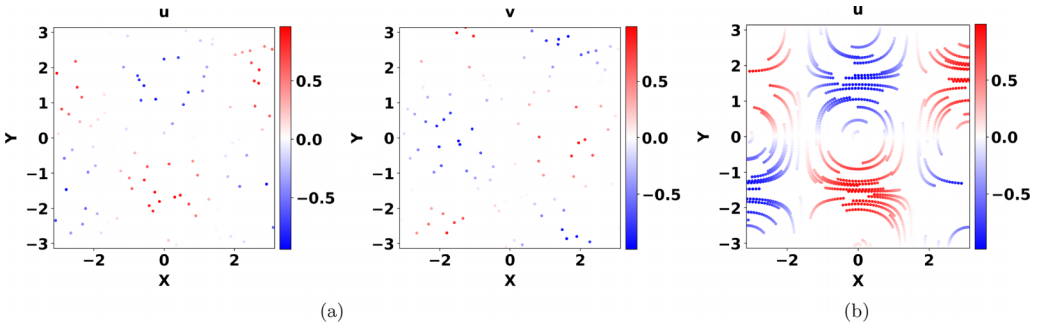

FIG. 5. Particle distribution and trajectories generated for the Taylor-Green vortex. (a) particle distribution and velocities of u and v; (b) particle trajectories.

vortex flow at one instant time step. The color map indicates the velocities of u and v of the particles. The velocities are translated from cylindrical coordinates to Cartesian coordinates to be consistent with other vortex models and also be easy to follow. These 100 points are randomly generated, and it can be seen that they are sparsely distributed in the domain. The domain size is $[-1, 1]$ in both x and y dimensions, the kinematic viscosity is set to 0.01, and the initial circulation strength Γ is set to 1. The time window is also $[0.1, 2]$ with a total of 21 steps. Note that the initial time here is not zero due to a singularity in the analytical solution, as shown in Eq. (5). At the initial time step, the particles are forced outside the core of the vortex, so the pressure distribution inside the vortex core is calculated based on the PDE residual only. Here only the particles inside the domain of interest are shown, and those outside the domain are omitted. For the Taylor-Green vortex and Lamb-Oseen vortex, the validation data are generated inside the same domain but with fixed Eulerian coordinates, with a fine resolution of 64×64.

Figure 7 shows the particle distribution at an instant time step. The entire time window is also $[0.1, 2]$ with a total of 21 steps. The flow domain size is $[-1, 1]$ in each dimension. The stretching rate $a = 0.1$, the circulation $\Gamma = 1$, and the kinematic viscosity $\nu = 0.01$. The density of particles is $10 \times 10 \times 10$, where 10 random coordinates are randomly generated on each dimension, respectively, and combined together, resulting in a total of 1000 sample points at each time step. For the validation data, the flow field is the same size but with a finer resolution of $64 \times 64 \times 64$.

B. Assimilation results of Taylor-Green vortex

The first case studied is the Taylor-Green vortex model, where the domain is set to be $[-\pi, \pi]$, with $U = 1$, $\rho = 1$, and $\nu = 0.01$. The density of training particles is 10×10, and the testing

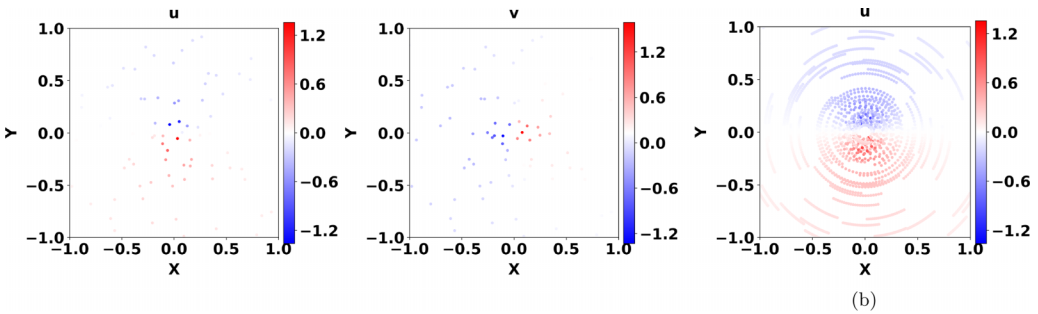

FIG. 6. Particle distribution and trajectories generated for the Lamb-Oseen vortex: (a) particle distribution and velocities of u and v; (b) particle trajectories.

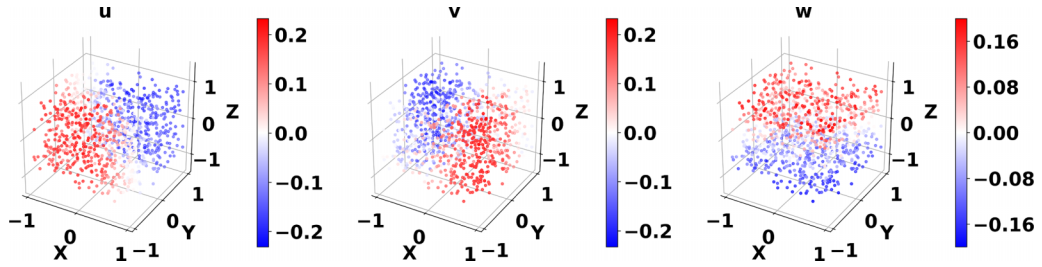

FIG. 7. Particles generated for Burgers' vortex at a certain time step.

resolution is 64×64. Figure 8 shows the velocity field reconstruction results and the comparison to the reference validation data. The outputs from PINNs are almost identical to the ground truth.

For the pressure field shown in Fig. 9(a), the prediction result from PINNs also matches well the reference ground truth. Figure 9(b) shows the pressure distribution along r, where the PINNs result (left) is nearly the same as the ground truth (right), although some tiny deviations can be observed, which make the result slightly noisier than the ground truth.

Overall, the flow field reconstruction results of PINNs for the Taylor-Green vortex show high accuracy. Table I summarizes the minimum pressure and errors in the prediction. The minimum pressure predicted by PINNs is very close to the reference value, and the overall $\mathcal{L}_2$ errors in all three fields are very small.

C. Assimilation results of Lamb-Oseen vortex

With the parameters set in Sec. II B, and the same density of sampled particles (10×10), the flow reconstruction results of the velocity fields are shown in Fig. 10. The results show a good agreement between the PINN model and the reference ground truth.

The pressure field results shown in Fig. 11 indicate that the PINN model prediction captures the patterns of the pressure field, where the minimum pressure point is located at the center of the domain, and the pressure values symmetrically diffuse along the r direction. Here only the pressure field at the initial time ($t = 0.1$) is shown since the pressure values increase over time, and the minimum pressure is obtained at the initial time. It is also observed that the prediction results for later steps show better performance than at the initial time since the pressure value is greater. Therefore, the minimum pressure value at the initial time is considered as a reference for evaluating the pressure field reconstruction performance. As shown in Fig. 11(b), the general trend of pressure distribution is well captured by PINNs, although the minimum pressure at the center is larger than the ground truth.

Table II summarizes the flow reconstruction results for the Lamb-Oseen vortex. The relative errors in u and v are still very small, while the errors in p are larger but acceptable. This is also

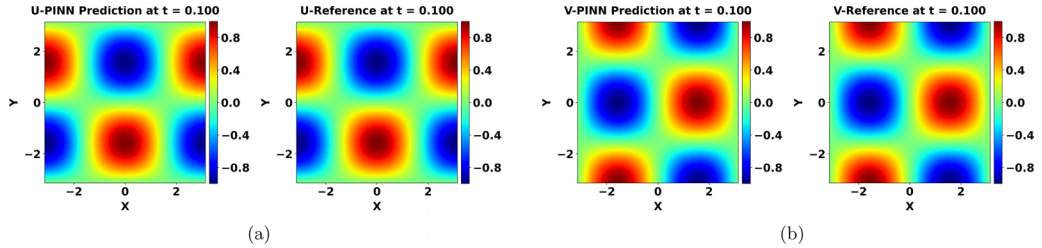

FIG. 8. Velocity field reconstruction of the Taylor-Green vortex: (a) u velocity; (b) v velocity.

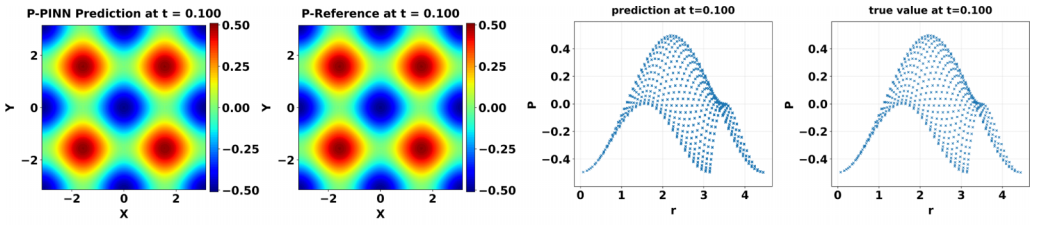

FIG. 9. Pressure assimilation results of the Taylor-Green vortex: (a) pressure field reconstruction; (b) pressure distribution.

revealed by the fact that the minimum pressure predicted by the PINN model is greater than the ground truth value.

D. Assimilation results of Burgers' vortex

The density of particles is $10 \times 10 \times 10$, and the reconstruction field has a resolution of $64 \times 64 \times 64$, which makes the observation rate as low as 0.38%. Since Burgers' vortex is steady, the choice of time step does not affect the results. In Fig. 12 the flow field reconstruction results are presented for the initial time step. The results show that, given the very low observation rate, the PINN model reconstructs the full 3D flow field with a 0.8% relative error in the pressure field compared to the reference ground truth.

To further examine the pressure field reconstruction results, Fig. 13 shows the pressure field and distribution along the r direction on the plane at $z = 0.02$. The prediction results match well the reference ground truth.

Table III provides quantitative results for the flow field velocities and the pressure. The minimum predicted pressure is nearly the same as the reference truth. The $\mathcal{L}_2$ relative errors are all almost negligible. These results indicate that even though the Burgers' vortex is a 3D problem, which is expected to be more complicated than the 2D problem, the PINN model can still successfully reconstruct the flow field from the sparse particle data. A possible reason could be that the Burgers' vortex is steady compared to the unsteady Lamb-Oseen vortex, which makes the problem easier to solve since the flow does not diffuse over time. Note that, although the Taylor-Green vortex is unsteady, the spatial variation remains the same.

E. Spatial and temporal convergence study

The previous sections present the flow field reconstruction results for all three canonical vortex flows at the initial time step. Similar comparisons are performed for the subsequent time steps to further examine the model's performance. Figure 14 shows the time histories of the errors in velocities and pressure. For the Burgers' vortex, the errors vary slightly within are less than 0.4%, since the Burgers' flow is a steady flow. The errors also slightly vary over a small range for the Taylor-Green vortex, and the errors in pressure are all less than 0.6%. For the Lamb-Oseen vortex, the pressure errors are higher at the initial time but then decrease significantly at all subsequent times. The larger pressure error observed at the initial time step is primarily due to the absence

TABLE I. Summary of the flow field reconstruction results of the Taylor-Green vortex.

$d^*_{nn}/\Delta x^*$	min p (ref)	min p (PINNs)	Errors in u	Errors in v	Errors in p
0.159/0.044	−0.498	−0.497	0.17%	0.17%	0.49%

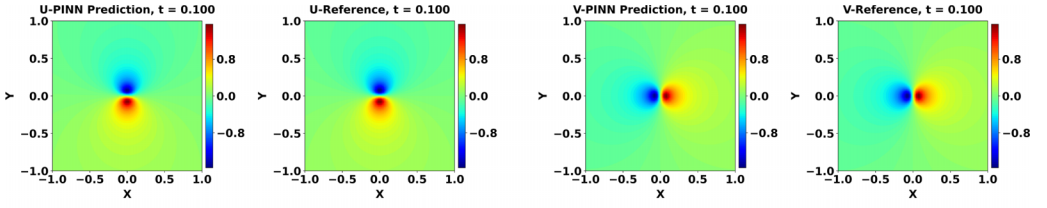

FIG. 10. Velocity field reconstruction of Lamb-Oseen vortex: (a) u velocity; (b) v velocity.

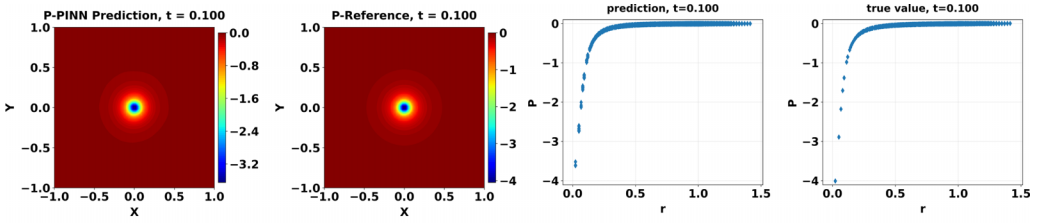

FIG. 11. Pressure assimilation results of the Lamb-Oseen vortex: (a) pressure field reconstruction; (b) pressure distribution.

TABLE II. Summary of the flow field reconstruction results of the Lamb-Oseen vortex.

$d^*_{nn}/\Delta x^*$	min p (ref)	min p (PINNs)	Errors in u	Errors in v	Errors in p
0.177/0.044	−4.0	−3.63	1.01%	1.32%	7.62%

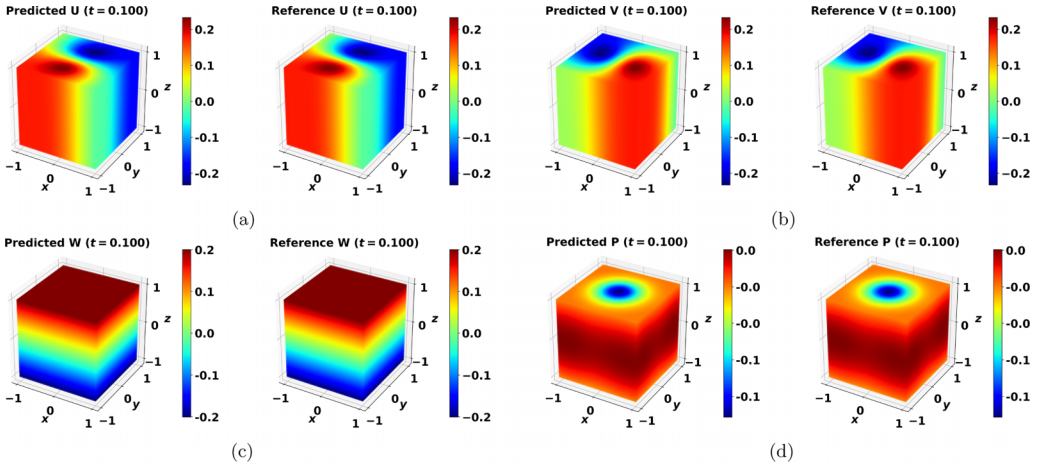

FIG. 12. Flow field reconstruction of Burgers' vortex: (a) u velocity; (b) v velocity; (c) w velocity; (d) p pressure.

TABLE III. Summary of the flow field reconstruction results of the Burgers' vortex.

$d^*_{nn}/\Delta x^*$	min p (ref)	min p (PINNs)	Errors in u	Errors in v	Errors in w	Errors in p
0.090/0.044	−0.0912	−0.0913	0.78%	0.11%	0.12%	0.32%

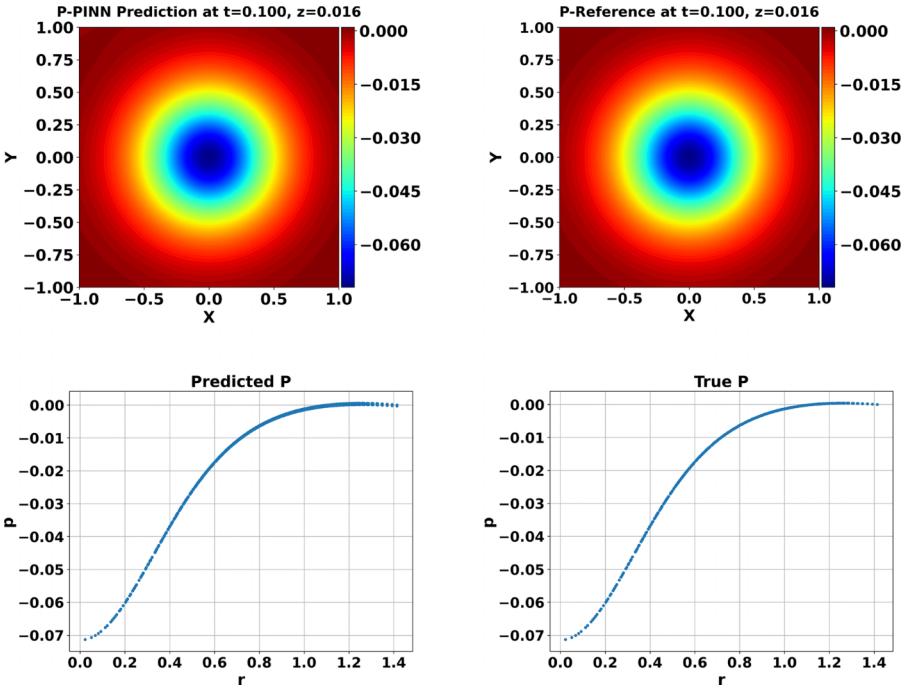

FIG. 13. Pressure distribution on a 2D plane of the reconstructed Burgers' vortex flow.

of velocity measurements within the vortex core. At early times, the pressure field inside the core is inferred solely from the PDE residual and the velocity information available outside the core. Specifically, the synthetic particles are initially placed outside the vortex core, defined by $r_c = \sqrt{4\nu t}$, and therefore no direct velocity data are provided within this region. As time increases, the vortex core expands radially while its peak magnitude decreases. Consequently, some of the previously placed particles gradually fall inside the vortex core. This provides additional velocity information within the core region at later times, which improves the pressure reconstruction. As a result, the pressure error at subsequent time steps is smaller than that at the initial time step.

The prediction results of the maximum and minimum pressure indicate the same trend as shown in Fig. 15. The predicted maximum and minimum pressures of the Taylor-Green vortex and the Burger's vortex agree well with the reference truth. For the Lamb-Oseen vortex, with the exception

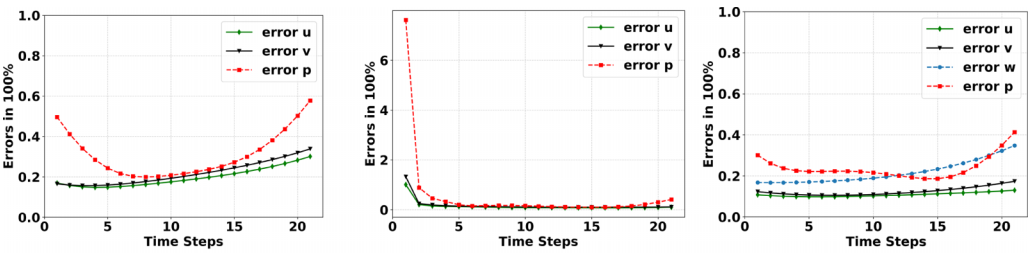

FIG. 14. Time histories of the prediction errors in velocities and pressure: (a) Taylor-Green; (b) Lamb-Oseen; (c) Burgers.

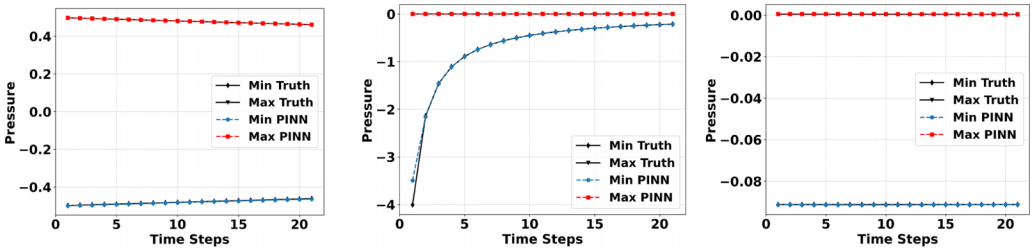

FIG. 15. Time histories of the maximum and minimum pressure: (a) Taylor-Green; (b) Lamb-Oseen; (c) Burgers.

of the initial time, all other time steps are well aligned with the reference value. Overall, the predicted values align well with the reference value at the given evaluation resolution.

The spatial resolution can impact the accuracy of computational results in traditional numerical methods. Therefore, a mesh convergence study is commonly used in computational fluid dynamics work. We also evaluate the analytical solution for the canonical vortex flows studied in this work, with the number of grids in one dimension ranging from [32, 64, 128, 256, 512], except for the Burgers' flow, where the largest number of grids is 256. The Taylor-Green vortex and Burger's vortex show that the minimum pressure is relatively invariant to the mesh size, where 32 grids are enough to obtain the minimum pressure. However, for the Lamb-Oseen vortex, the minimum pressure highly depends on the grid size. However, one of the benefits of PINN is that, once the model is trained, it can be directly evaluated for the same problem at various resolutions. Here we evaluated the pretrained PINN model for the Lamb-Oseen vortex based on 10×10 sparse particle observation at all the above resolutions, where the computation time is within a few seconds.

Table IV summarizes pressure prediction results for the Lamb-Oseen vortex at various spatial resolutions. The referenced minimum pressure evaluated at different resolutions shows a decreasing trend with the increase in the number of grids, i.e., smaller minimum spatial distance. When the grids increase from 32 to 64, the minimum pressure significantly decreased from -3.09 to -4.0. The minimum pressure shows a converged trend when the number of grids is larger than 256. The minimum pressure predicted by the PINN model also shows the converged trend at finer resolution; however, a constant deviation can be observed since the minimum pressure is -3.87 at 512×512, while the reference value is -4.37. These results show that the PINN model can reconstruct the flow field at various resolutions, with convergence at a finer scale, and the computational cost is negligible. The L_2 relative errors for the pressure in the entire domain remain at the same level across different resolutions, indicating the robustness of the PINN model for this problem.

IV. SENSITIVITY OF MODEL PERFORMANCE TO SAMPLE DENSITY, DISTRIBUTION, AND NOISE

Section IV A investigates the effects of sampled particle density and distribution on the PINN model's prediction accuracy using the Lamb-Oseen vortex flow. A partial-observability case is also

TABLE IV. Minimum pressure prediction results on various spatial resolution, Lamb-Oseen vortex.

Resolution	32×32	64×64	128×128	256×256	512×512
Δx^*	0.088	0.044	0.022	0.011	0.006
min p PINN	-2.91	-3.63	-3.82	-3.86	-3.87
min p Ref	-3.090	-4.0	-4.29	-4.35	-4.37
L_2 errors	7.15%	7.62%	7.75%	7.74%	7.78%

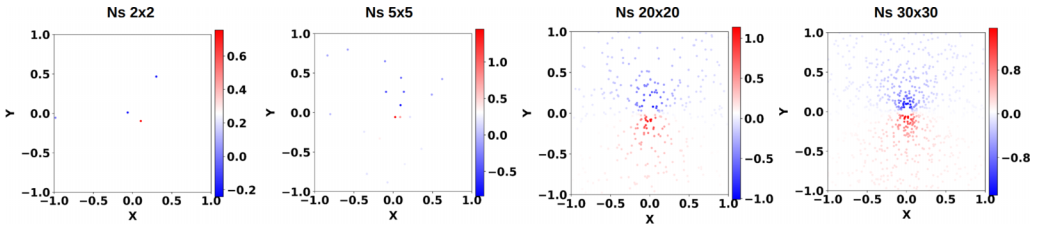

FIG. 16. Illustration of different particle densities of the Lamb-Oseen vortex.

discussed, in which we use down-sampled 2D velocity data from a 3D Burgers' vortex flow to estimate the corresponding pressure field. This section also discusses the effects of the sampling noise for all three vortex models.

A. Sensitivity to sample density and distribution

As discussed in the introduction, the particles might be sparse at some vortex locations in the experiments [3], which results in a low accuracy of the flow measurement. We therefore explore the sensitivity of the PINN model performance for different particle densities on the accuracy of the assimilated minimum pressure. In Sec. III the result of the Lamb-Oseen vortex flow has slightly larger errors than the other two. Therefore, we investigated the sensitivity of the PINN model to the sample density using the Lamb-Oseen vortex alone. The particle densities are selected as 2×2, 5×5, 10×10, 20×20, and 30×30. Figure 16 shows the visualization of different particle densities, except 10×10, which has been shown in Fig. 6. As shown in Table V, the density of 2×2 gives an average nondimensional distance d_{NN} of 0.672, while the densest case yields an average distance of 0.059.

The numerical experiments cover all five cases above. For each case, the model is trained with the same manually set learning rate schedule and the total number of iterations. In addition to the sampled particles, 30 000 additional points are collected as collection points to compute the physical loss of the PINN model only. So the data loss computes the MSE in velocities for the sampled particles, and the physical loss computes the MSE of both the sampled particles and the additional collection points. The results are summarized in Table V. In general, the errors in pressure decrease when the particle densities increase. The same trend is observed in the minimum pressure. The lowest density case has only four particles at each time step, but the results are still acceptable, which gives the minimum pressure value of -3.53. When the density goes to 30×30, the errors in p do not decrease much, but the minimum pressure is much closer to the reference truth -4.0. Figure 17 shows the pressure field reconstructed at different densities. The key features are well captured by the PINN model, so the errors may mainly be caused by the differences in the minimum pressure at the core location. For the velocities, the results are generally good across all cases, with the higher density showing smaller errors and more accurate minimum and maximum

TABLE V. Summary and comparison of the flow field reconstruction and minimum pressure estimation results at $t = 0.1$ for different particle densities.

Density of particles	d^*_{nn}	min p	Errors in p	Errors in u	Errors in v
2×2	0.672	-3.53	12.18%	7.94%	8.27%
5×5	0.365	-3.63	10.05%	2.08%	2.44%
10×10	0.177	-3.69	6.70%	1.01%	1.33%
20×20	0.091	-3.78	3.63%	0.62%	0.57%
30×30	0.059	-3.93	2.44%	0.29%	0.33%

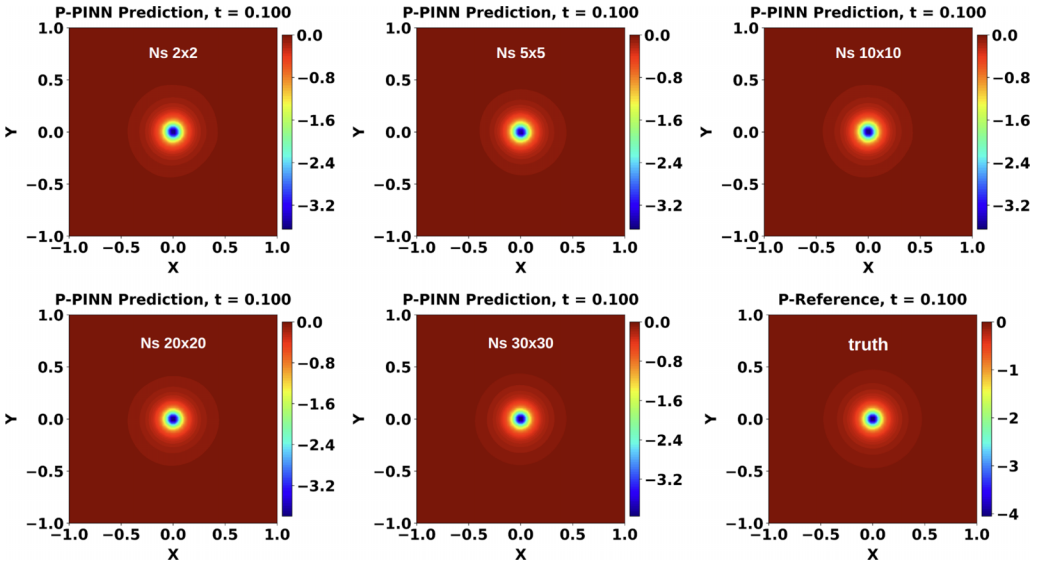

FIG. 17. Pressure field reconstruction for different particle densities.

velocities in u and v. Even for the lowest density 2×2, the errors in the velocities are around 8% only. These results reveal that the PINN model performs very well in interpolation tasks. For the minimum pressure estimation, the higher density provides a more accurate prediction.

The above results are based on a random distribution of particles, where the initial spatial coordinates are generated using a Latin Hypercube Sampling (LHS) method. However, in the experiments the initial particles can also be distributed uniformly. Therefore, we test the model's performance using three densities 2×2, 10×10, and 30×30. For each case, the particles are uniformly distributed in polar coordinates. For example, in 10×10 case, the angular coordinate θ is uniformly sampled in the interval $[0, 2\pi]$, while the radial coordinate r is uniformly sampled between r_c and $r_{\max}$ using 10 radial levels. At each radial level, 10 particles are placed with uniform angular spacing. Figure 18 shows the uniform particle distributions at initial and last time steps, for 10×10 and 30×30 cases.

The training details are exactly the same as the previous test cases, as are the neural networks' hyperparameters. The flow field reconstruction results are summarized in Table VI. For the 2×2 case, the uniform distribution shows slightly worse prediction than the random case, with higher errors in pressure and velocity, although the minimum pressure is slightly closer to the reference value. This is because the uniform distribution in this case contains only two particles right outside the core and two at the domain's maximum radius, whereas the random distribution has two particles closer together. The 10×10 case shows better performance on both minimum pressure and the

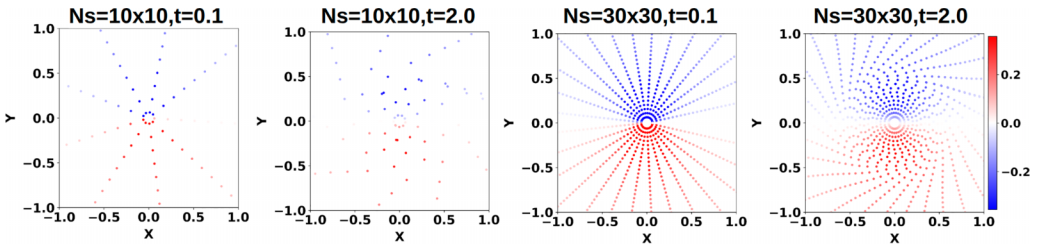

FIG. 18. Illustration of uniform distribution particles at the initial and last time with different densities.

TABLE VI. Summary and comparison of the flow field reconstruction and minimum pressure estimation results at $t = 0.1$ for uniformly distributed particles.

Density of particles	Distribution	min p	Errors in p	Errors in u	Errors in v
2×2	Uniform	-3.55	12.97%	8.74%	8.71%
10×10	Uniform	-3.76	9.07%	0.47%	0.48%
30×30	Uniform	-3.79	7.86%	0.37%	0.30%

general relative errors of the pressure and velocity fields. However, as the particle density increases, the improvement in model performance is very limited. The 30×30 case has a worse performance than the randomly sampled particles.

B. Incomplete velocity measurements for 3D vortex flow

Another practical experimental setting considered in this section is an incomplete velocity measurement problem, where the 2D PIV data are collected from a 3D flow, with missing velocity components. We use the Burger's vortex flow for this test case. The training data are sampled from a single x-y plane at the middle of the z axis with a mesh resolution of 64×64. The training data are down-sampled to $1/10$ of its original size. The training data are therefore u, v at the corresponding particle coordinates. The time window is set to the same as the previous test case in Sec. III. The model has three inputs, x, y, t, and three outputs, u, v, p, with eight hidden layers and 100 neurons per layer. The physical equations used for this case are the 2D incompressible Navier-Stokes equations. This case is challenging because the Burgers' vortex flow is an analytical solution to the 3D incompressible Navier-Stokes equation, but not to the 2D one. Therefore, it is worthwhile to test the PINN model's performance in such a partial-observation scenario and to reconstruct the flow field using incomplete velocity measurements and an inaccurate physical equation.

Figure 19 shows the flow field reconstruction results of such an incomplete velocity problem. Obvious deviations can be seen for all the flow fields, especially for the velocity fields near the boundary of the domain and the location of the minimum and maximum velocities. However, the pressure field is still reconstructed by the PINN model, particularly the radiant patterns and the low pressure at the domain center. The deviation at the boundary can also be observed

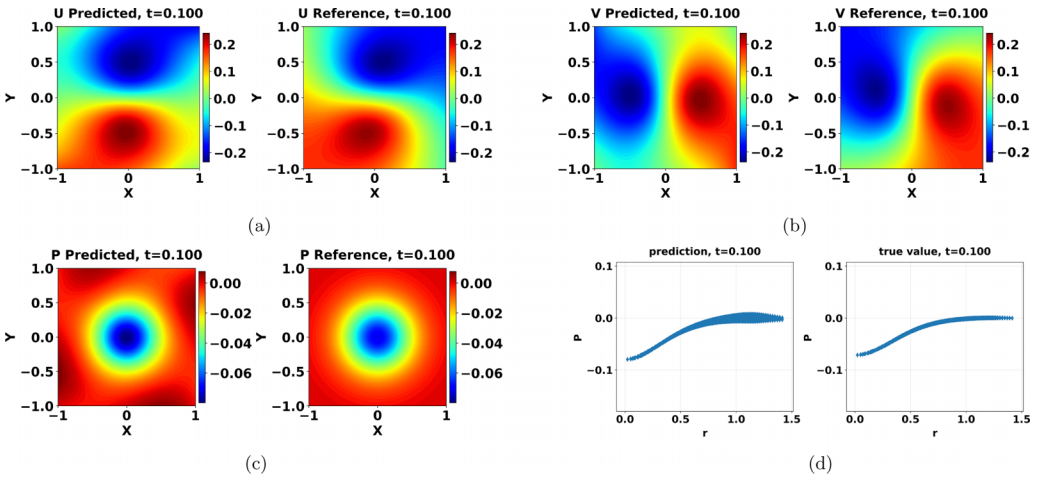

FIG. 19. Flow field reconstruction of the incomplete 2D Burgers' vortex. (a) u PINN (left), reference (right). (b) v PINN (left), reference (right). (c) p PINN (left), reference (right). (d) p distribution.

TABLE VII. Quantitative results of the incomplete 2D Burgers' vortex.

min p (ref)	min p (PINNs)	Errors in u	Errors in v	Errors in p
−0.071	−0.079	31.06%	31.01%	13.61%

in the reconstructed pressure field, which can be caused by the errors in the predicted velocities. The pressure distribution in Fig. 19(d) shows a good agreement of the minimum pressure with the reference solution.

The errors in Table VII show that the reconstructed pressure field has a relative error of 13.61%, which is lower than the velocity fields at 31%. Interestingly, the reconstructed pressure field exhibits higher accuracy than the velocity field. This behavior can be attributed to the strong physical constraints imposed by the governing Navier-Stokes equations, which tightly couple pressure to the velocity gradients. In addition, the pressure field is generally smoother than the velocity field, making it easier for the neural network to approximate. These results suggest that a physics-informed learning model can effectively infer pressure from incomplete velocity measurements, at least for the test case in this work.

C. Sensitivity to sampling noise in velocity

Previous results show that the PINN model performs well on synthetic particle data. In real-world experiments, however, the particle measurements could be noisy for multiple reasons. Therefore, it is important to explore the model's performance with uncertainties and study the PINN model's sensitivities to different noise levels. This section presents the flow field reconstruction results from noisy data, where Gaussian white noise is added to the velocity data for training. The noisy velocities are studied for all three vortex flows. Here we use the Burgers' vortex as an example where the noisy velocities are defined as

$$\bar{u} = u + \epsilon_u, \quad \bar{v} = v + \epsilon_v, \quad \bar{w} = w + \epsilon_w, \quad \text{where } \epsilon \sim \mathcal{N}(0, \sigma). \tag{11}$$

Three different noise levels are tested, $\sigma = 0.01$, $\sigma = 0.05$, and $\sigma = 0.1$, which correspond to small, medium, and heavy noise, respectively. The same approach is applied to the noise of spatial coordinates, so that the equations are omitted here. Tests are run for all three vortex models, and for each noise level and vortex model, three runs are used to check the uncertainties due to the noise and to better examine the performance of the PINN model. It should be noted that the present study does not aim to perform a formal uncertainty quantification analysis. Instead, the noise perturbations are introduced to illustrate the sensitivity of the proposed method to potential measurement noise and to qualitatively assess its robustness. To focus on aleatoric uncertainty from measurement noise alone, we used the same seed for each noise level to train the model, so that we could prevent implicit epistemic uncertainty arising from training progress, such as neural network parameter updates and collocation-point sampling. All the flow parameters are set the same as Sec. III, and the low density (10 points in each coordinate) of particles is used.

Figure 20 shows the comparison of the velocity histories of a single particle at different noise levels. When the noise level σ increases, significant changes and disturbances in the velocity can be seen. For heavy noise, the time history trajectory looks very different from the clean data without noise. The pressure field reconstruction results for the Taylor-Green vortex at different noise levels are shown in Fig. 21. The results indicate that even for heavy noise, the PINN model can still reconstruct the pressure field with reasonable accuracy. For the specific value of the minimum pressure and the relative errors in velocities, Fig. 21(b) shows the results of all three runs, where the upper and lower bar is the upper and lower values of the minimum pressure in the reconstructed pressure field, and the black dot is the mean value among the three runs. This figure shows the model's sensitivity to the estimated minimum pressure across three noise levels. The same legend is used to denote the corresponding quantities in Figs. 22(b) and 23(b) for the Lamb-Oseen vortex and

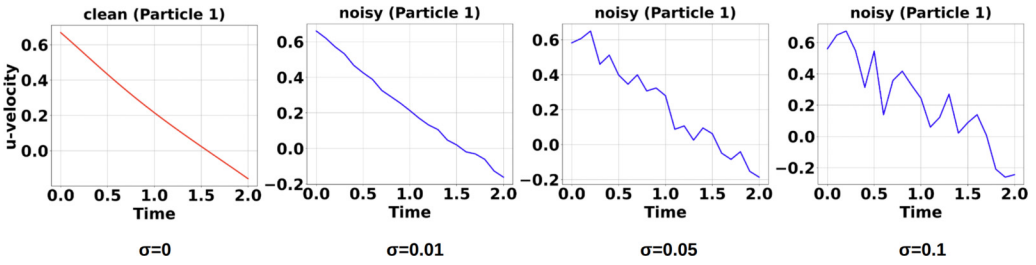

FIG. 20. Velocity histories of a single particle of the Taylor-Green vortex.

Burgers' vortex, respectively. Figure 21(c) shows the average errors in velocities and pressure. For the minimum pressure, the larger noise level has a larger influence on the variance of the prediction results; however, the values in general do not deviate much from the ground truth. The average errors of velocities are less than 4.5% even for the heavy noise level, with a general increasing trend aligned with the level of noise. The average error of the pressure field also increases with the level of noise; however, it surges from 6% to 16% when the noise increases.

The results for the Lamb-Oseen vortex and Burgers' vortex are shown in Figs. 22 and 23, respectively. A no-noise case is also included as the control group. The same trend in the sensitivity of reconstructed minimum pressure to the noise levels can be seen for both of them. When the noise level is higher, the minimum pressure has a larger variance, which could even result in a

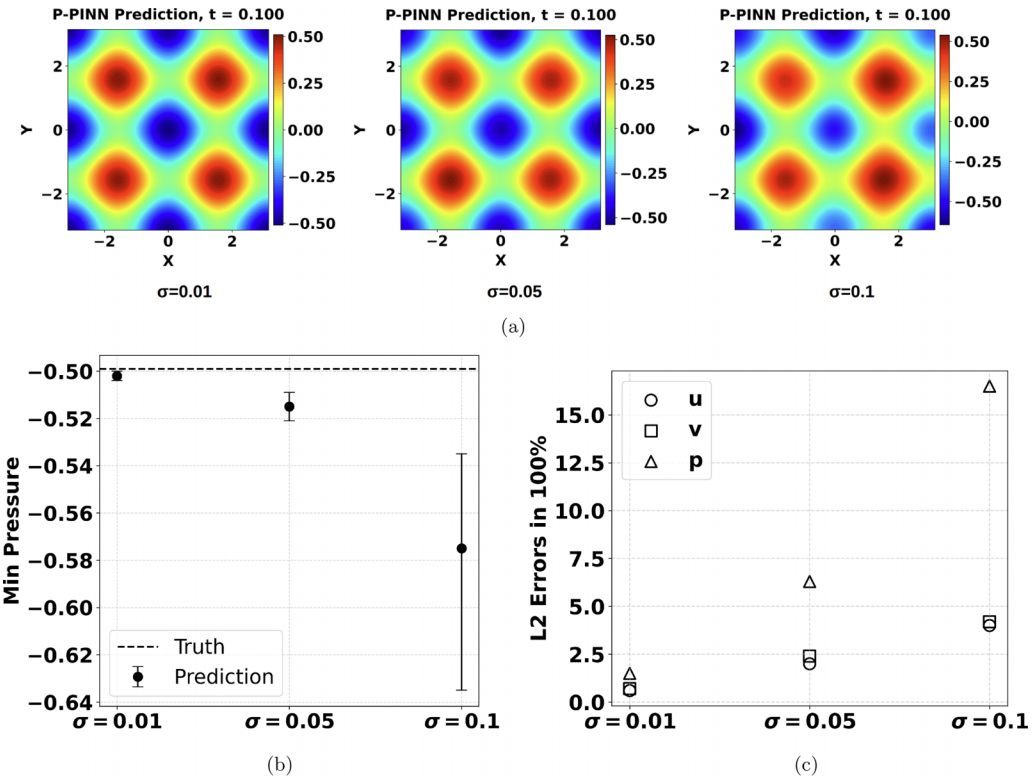

FIG. 21. Pressure field reconstruction results for different noise levels, Taylor-Green vortex: (a) pressure field reconstruction; (b) minimum p; (c) errors in average.

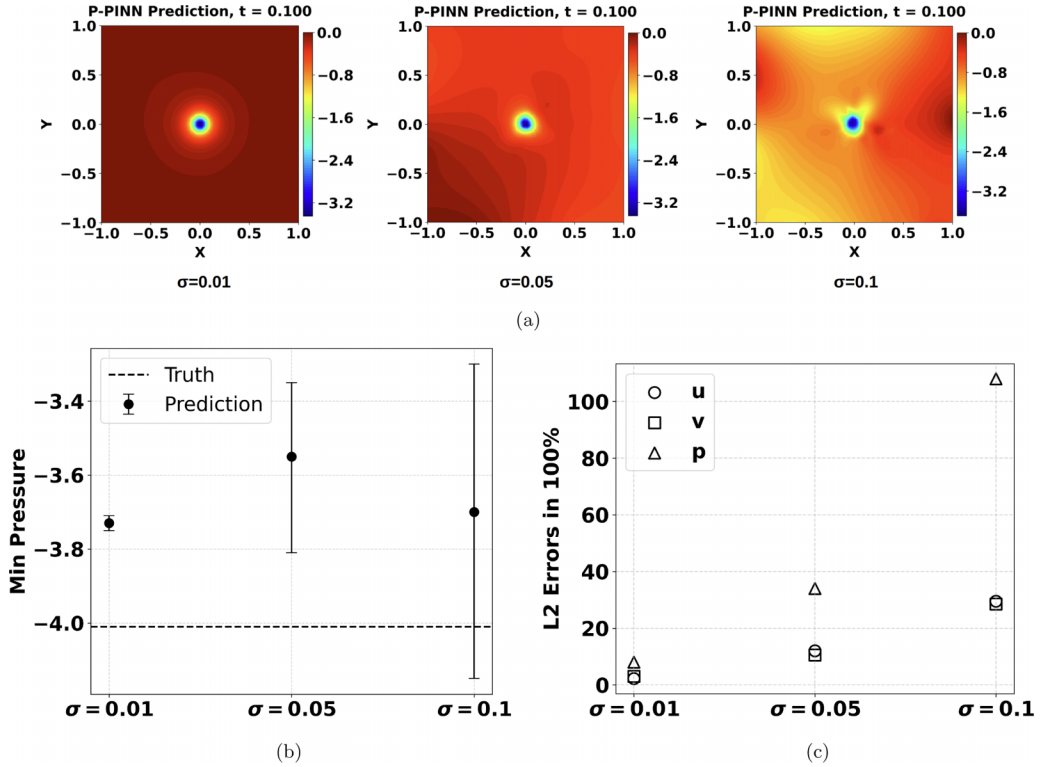

FIG. 22. Pressure field reconstruction results for different noise levels, Lamb-Oseen vortex: (a) pressure field reconstruction; (b) minimum p; (c) errors in average.

minimum pressure lower than the reference value when the noise is heavy. The errors of velocities for the Lamb-Oseen vortex, however, could be very large in heavy noise data, although the estimated minimum pressure is stable. The reconstructed pressure fields of the Lamb-Oseen vortex shown in Fig. 22(a) indicate that, although the PINN model correctly captures the location of the minimum pressure, the overall structure and spatial distribution of the pressure field deviate from the reference solution. As the noise level increases, this discrepancy becomes more pronounced, as illustrated in Fig. 22(c). In particular, the reconstructed pressure field becomes progressively smoother and fails to recover the expected radial pressure distribution characteristic of the Lamb-Oseen vortex. The relatively stable estimation of both the minimum pressure and its location can be attributed to the absence of measurement particles within the vortex core, where the minimum pressure occurs. Because no particles are placed in this region, the injected noise in the velocity measurements does not directly contaminate the information within the vortex core. Consequently, the pressure reconstruction in this region is primarily governed by the governing equations rather than noisy observations. In contrast, outside the vortex core, where particles are present, the added noise in the velocity data can introduce erroneous information to the model and lead to larger deviations in the reconstructed flow quantities. As a result, the minimum pressure and its location remain comparatively robust to measurement noise. For the Burgers' vortex, the results are generally good for all pressure fields, the minimum pressure, and the errors in velocities.

In general, the PINN model shows robustness to the velocity noise for all three vortex flows, for standard deviation $\sigma = 0.01$ and 0.05, for $\sigma = 0.1$, the Taylor-Green vortex and Burgers' vortex still have good results, but the Lamb-Oseen vortex shows large error. The minimum pressure, however, is still in an acceptable range even for the worst case.

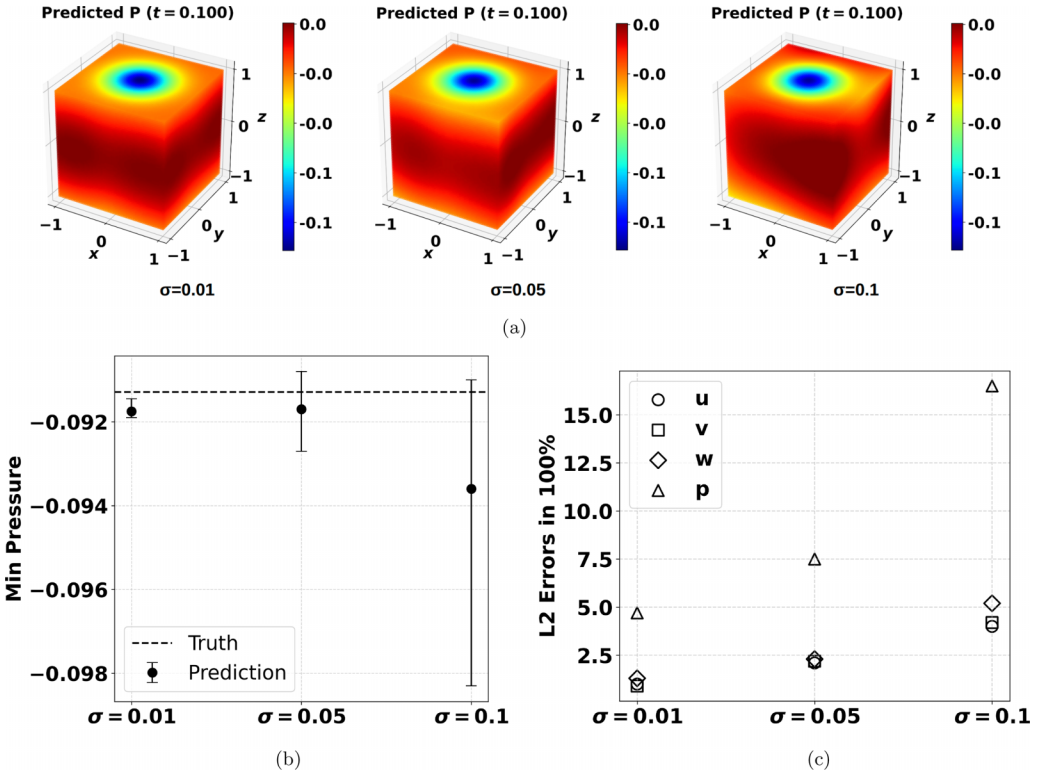

FIG. 23. Pressure field reconstruction results for different noise levels, Burgers' vortex: (a) pressure field reconstruction; (b) minimum p; (c) errors in average.

D. Sensitivity to sampling noise in spatial coordinates

All three vortex models are examined for the effects of noise in spatial coordinates. Figure 24 shows two examples of the spatial noise and the particle distributions for different noise levels. When the noise level is low, the trajectories are very close to the noise-free case, but the particles show large deviation when the noise is heavy.

The flow field reconstruction results are summarized in Fig. 25. For each noise level, a total of three runs were used to test the uncertainty. The minimum pressure values at different noise levels for the three vortex models are shown in Figs. 25(a), 25(c), and 25(e). As expected, the values of minimum pressure deviate more when the noise levels are higher; however, the variations in each case do not have a clear increasing trend with the noise level, like that observed in the velocity noise. For the Taylor-Green vortex, higher noise levels produce smaller minimum pressure, but the Lamb-Oseen vortex and Burgers' vortex show the opposite results: the higher noise levels give larger minimum pressure. The predictions of the Taylor-Green vortex and the Burgers' vortex are more robust among different noise levels in spatial measurements, especially for the Burgers' vortex, where the effects of the spatial noise at small and medium levels are nearly negligible. Similar to the velocity noise, higher noise levels give larger deviations of the minimum pressure from the reference truth. However, the Lamb-Oseen vortex shows poor performance even in the medium spatial noise. The average errors (in three runs) of the reconstructed velocity fields and pressure fields are shown in Figs. 25(b), 25(d), and 25(f). In general, the errors of pressure are always higher than the errors of velocity, and the errors increase with the noise level. Lamb-Oseen vortex showed the least robustness to the spatial noise, where the errors of pressure go up to 70% for heavy noise and 50% for medium noise. The Taylor-Green vortex and Burgers' vortex are generally more robust

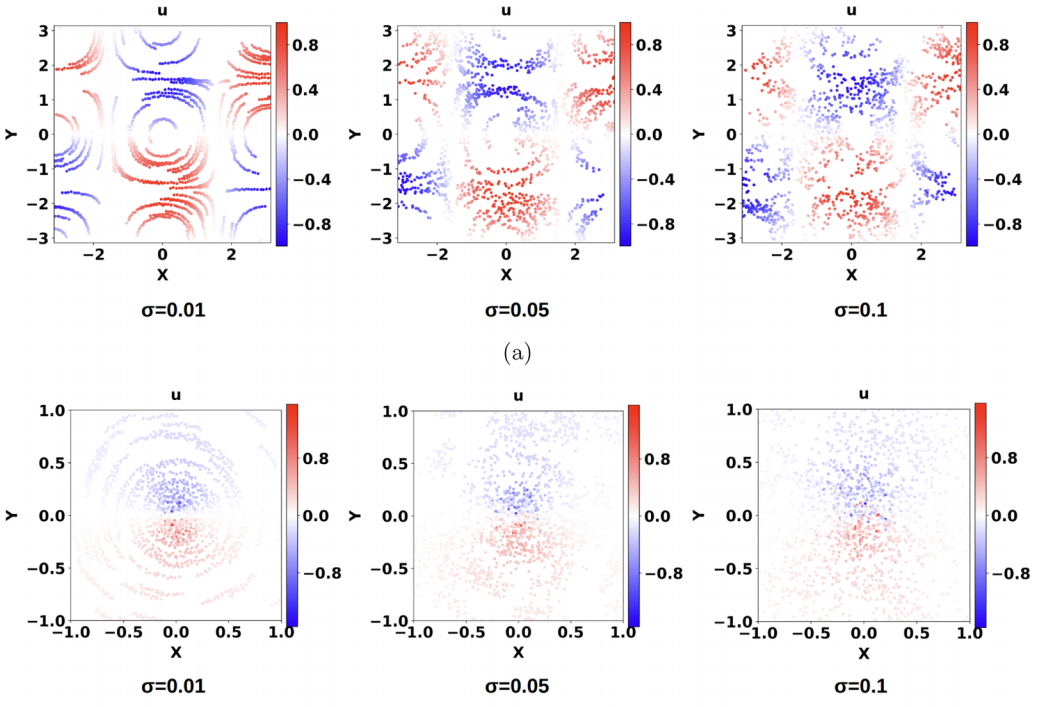

FIG. 24. Visualization of the spatial coordinates noise at different levels: (a) trajectories of Taylor-Green vortex; (b) trajectories of Lamb-Oseen vortex.

even in the heavy noise; the errors of pressure rise to 14% for the Taylor-Green vortex and only 8% for the Burgers' vortex.

The spatial noise shows less variance across the different noise levels, in comparison to the velocity noise. The minimum pressure and errors for the Taylor-Green vortex and Burgers' vortex are very close to the values in velocity noise. However, the minimum pressure for the Lamb-Oseen vortex is worse when $\sigma = 0.05$ and 0.1, which is worse than all the cases in the velocity noise. The results indicate that spatial noise can severely influence the flow field reconstruction and pressure assimilation accuracy for vortex flows.

V. TEST ON TURBULENT COUNTERROTATING VORTICES OF UNEQUAL STRENGTH

The proposed framework is tested using an incompressible turbulent flow database [21] obtained using the large-eddy simulation (LES) method. The problem involves two hydrofoil-generated counterrotating vortices of unequal strength. The weaker vortex is stretched by the stronger vortex, leading to a significant drop in pressure that could cause cavitation inception. Such interactions are central to cavitation inception [22] in ducted propulsors [4]. The dataset used in this work does not have cavitation. For more details of the data generation, refer to [21]. The data are organized as multiple 2D slices in the y-z plane, from 1 to 20 at an axial distance of 0.01 in the x direction. The time step size is 0.005 time units. The kinematic viscosity is 1×10^{-6}, and the reference velocity is 10 m/s, length of 0.167 m, and density of 1000 kg/m^3, which results in a Reynolds number of 1.67×10^6. To mimic the sparse measurements, the training data sample the velocities with a down-sample size of 1/20 while the full-size data are used as the validation data. We aim to reconstruct the resolved flow field, assimilating the pressure field, from the sparse training data.

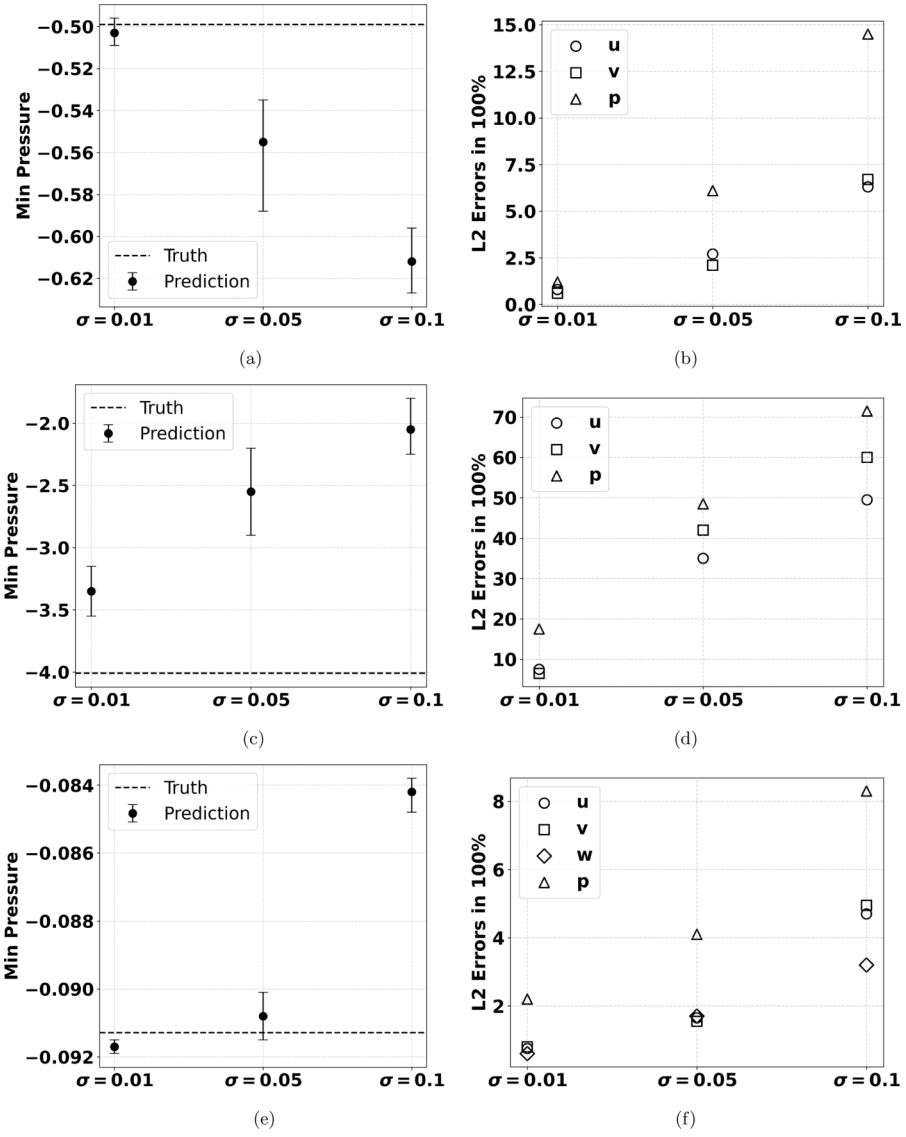

FIG. 25. Sensitivity to spatial coordinates noise in minimum pressure and quantified errors. (a), (b) Minimum p, Taylor-Green. (c), (d) Minimum p, Lamb-Oseen. (e), (f) Minimum P, Burgers.

The training and validation process of PINN is run on the same NVIDIA A100 GPU, based on the Python open-source library TensorFlow2. The hidden layers of the neural network for this problem were set to be eight layers with 200 neurons per layer. The activation function is the hyperbolic tangent function tanh, and we used the same loss weight λ for the data and PDE loss. The input coordinates of the training data are normalized by the min-max value. The total training epochs are set to 2000, with a validation frequency of 100 epochs. The PDE equation used for training is the same as Eq. (2), i.e., a 3D incompressible Navier-Stokes equation. In this problem, we selected the collocation points using the same coordinates as the down-sampled training data points, resulting in a total of $N_s = 521\,690$ sampled data points and $N_f = 521\,690$ collocation points over 10 time steps.

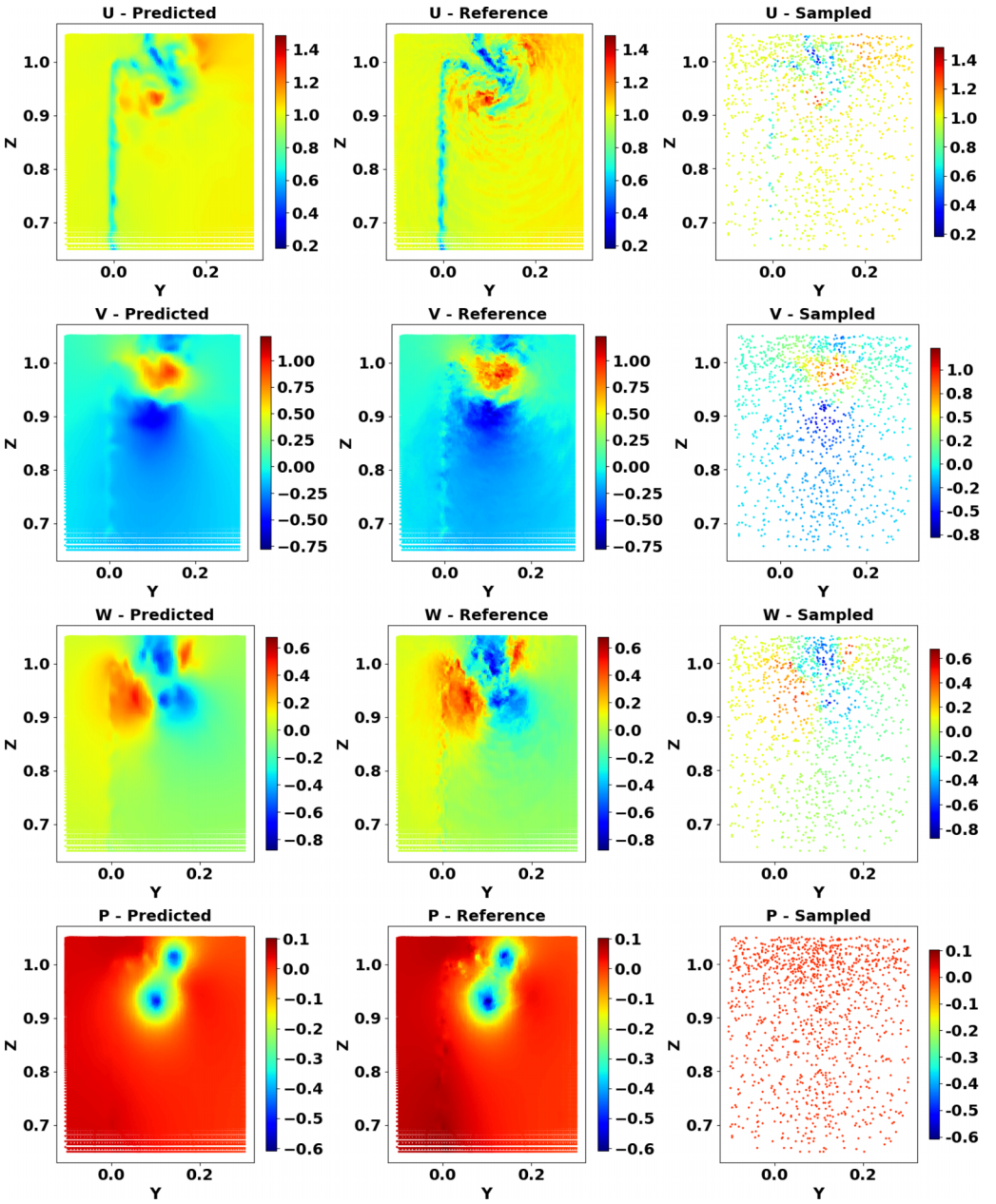

FIG. 26. Comparison of the results in 2D y-z plane slice at $t^* = 2$: LES (left), PINNs (middle), sample (right).

We used a gradient-balancing method introduced by [23] during model training. The validation dataset contains four time steps due to GPU memory limitations.

The results are shown in Figs. 26 and 27 along with multiple 2D slices in y-z plane and x-y plane, respectively. Here we use the second time step as an example. The left columns of each subfigure display LES simulation results, and the right columns show the down-sampled data points used for training at the corresponding slice. The pressure values in the training data are set to zero to

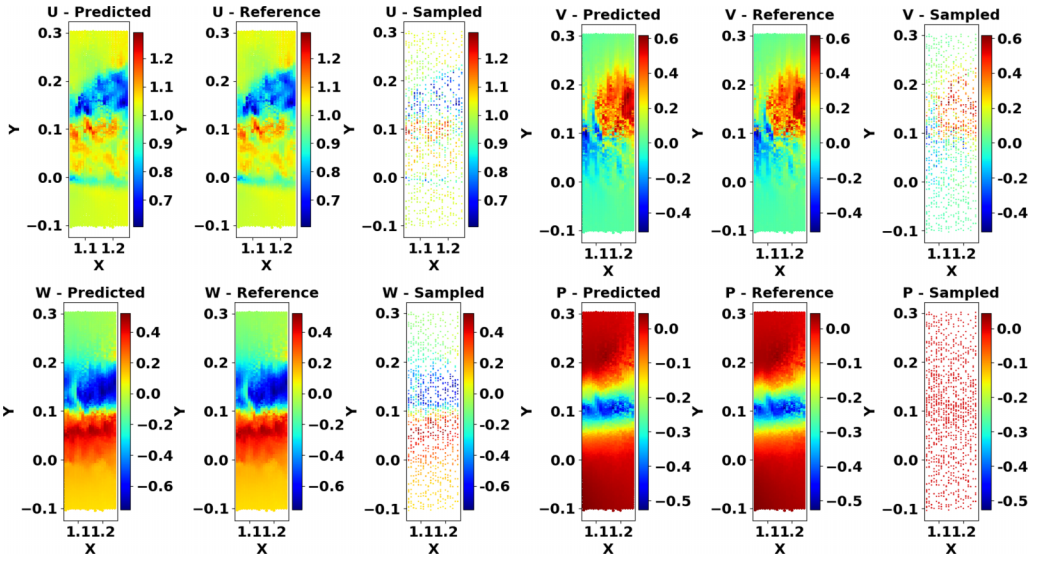

FIG. 27. Comparison of the results in 2D x-y plane slice: LES (left), PINNs (middle), sample (right).

prevent data leakage. The LES simulation data contain multiple 2D y-z planes in the x direction with constant spacing and are significantly larger than the distances in the y and z directions; therefore, the data are downsampled on each y-z plane. The reconstruction results predicted by the PINN model are shown in the middle columns of each subfigure. It can be seen that the reconstructed results are close to the LES simulation results. The flow fields reconstructed by the PINN capture the overall patterns of the turbulent flow and also indicate the locations of the twin vortices, as shown in the pressure field.

The flow fields reconstructed by the PINN model are generally smoother than the LES results, especially for the velocity field. The $\mathcal{L}_2$ error of the entire flow field over the entire simulation time is computed and summarized in Table VIII. The minimum pressure obtained in the prediction is 0.525, which is slightly higher than the LES results, 0.612. Although the error in the u velocity field has a larger error, the other three fields have significantly lower errors, especially for the pressure field with a relative error as low as 1.65%. A possible reason that the u velocity has a higher error could be that the density of the particles in the x direction is also much lower than in the other two directions.

The test of turbulent flow shows that the PINN model can also reconstruct the flow field of turbulent flow at high Reynolds numbers and assimilate the pressure field from sparse measurements. The pressure field error is small, and the minimum pressure assimilated is close to the reference value of LES. The results from PINN are generally smoother than those from LES. This could be caused by the spectral bias, which is a common issue for neural networks [24]. The velocity in x the direction is less accurate than the other quantities, as the particle density is significantly smaller in this direction, which agrees with the results discussed in Sec. IV A.

Further insight is provided by the probability density functions (PDFs) of the time-averaged turbulent kinetic energy k shown in Fig. 28(a), with the LES reference solution, down-sampled training

TABLE VIII. Summary of the flow field reconstruction for twin-vortex simulation.

Error in u	Error in v	Error in w	Error in p	min p prediction/truth
23.43%	4.83%	5.08%	1.65%	−0.525/−0.612

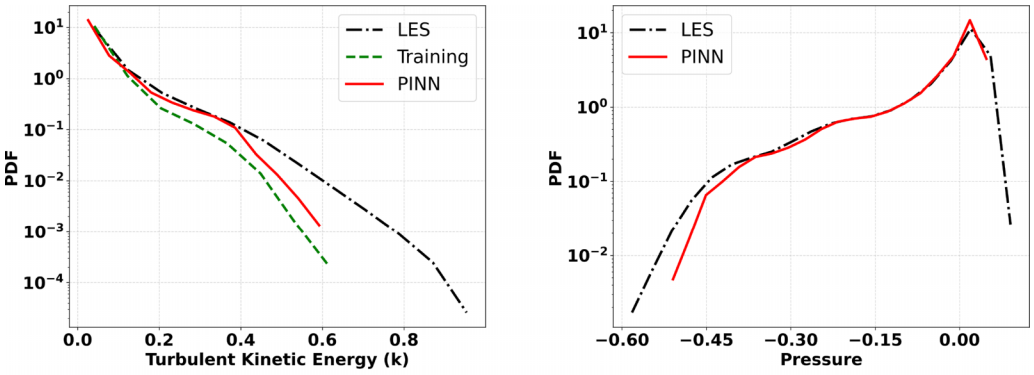

(a) (b)

FIG. 28. Comparison of the PDFs of LES reference solution, training data, and reconstructed results of PINN for the turbulent kinetic energy (left) and pressure (right).

data, and the reconstructed results of PINN model. The down-sampled training data under-represent the high-energy portion of the distribution, indicating that the measurement particles provide limited sampling of energetic turbulent structures. Despite this limitation, the PINN reconstruction recovers the overall statistical shape of the LES distribution across a broad range of k, demonstrating that the physics-constrained learning framework is capable of inferring missing flow statistics beyond the available observations. In particular, the agreement between the PINN and LES curves in the intermediate energy range suggests that the governing equation constraints help regularize the reconstruction and propagate physically consistent information throughout the domain. However, discrepancies remain in the high-energy tail of the PDF, where the PINN under-predicts the probability of extreme events. This behavior is expected because intermittent high-energy structures are both rare and weakly constrained by the available measurements. It also supports the previous discussion about the spectral bias of neural networks, which tend to preferentially learn low-frequency components of the solution. As a result, intermittent high-frequency flow structures associated with extreme turbulent events may be insufficiently represented in the reconstructed field.

Figure 28(b) compares the PDFs of pressure obtained from the LES reference solution and the PINN reconstruction, since pressure is excluded in the training data. Overall, the PINN model also captures the main statistical structure of the pressure distribution across most of the range. In particular, the agreement between the two curves in the central portion of the distribution indicates that the PINN is able to reproduce the dominant pressure fluctuations associated with the bulk turbulent motions. However, noticeable discrepancies appear in the tails of the distribution. The PINN model under-representing the extreme negative-pressure events observed in the LES data is also shown in Table VIII. These deviations are likely associated with the limited sampling of intense turbulent structures and the smoothing tendency of PINN reconstructions. Consequently, while the PINN framework reproduces the overall pressure statistics reasonably well, accurately capturing rare extreme events remains more challenging. Overall, the results indicate that while sparse training data alone do not capture the full turbulence statistics, the PINN framework can recover much of the underlying statistical structure through the incorporation of physical constraints.

VI. CONCLUSIONS

This work demonstrates the ability of machine learning methods, in particular Physics-Informed Neural Networks (PINNs), to reconstruct fine-resolution flow fields from sparse and noisy measurements. Using several analytical vortex models in both two and three dimensions as test cases, this study systematically evaluated the performance of the proposed method in reconstructing both

velocity and pressure fields and obtaining the location and value of the minimum pressure from sparse and noisy measurement data.

The model is first tested with synthetic sparse particle data generated from the solutions of the analytical vortex flows. For the Taylor-Green and Burgers' vortex models, the reconstructed velocity and pressure fields closely match the reference truth, including accurate identification of the minimum pressure. Although the Lamb-Oseen vortex case exhibited slightly higher errors, particularly for pressure prediction, these errors remain within an acceptable range. The temporal study shows that the accuracy for the Taylor-Green vortex and Burgers' vortex remains within a similar range over time. The Lamb-Oseen vortex errors are initially higher but decrease significantly to small values in subsequent time steps. The resolution convergence study indicates that the minimum pressure for the Lamb-Oseen vortex depends on resolution, but it converges as the grid size becomes sufficiently small, as observed in the PINN model predictions. The trained PINN model can easily compute the pressure field for various resolutions, demonstrating the potential benefits in real applications. However, the PINN model is indeed different from some data-driven models that can be directly applied to similar problems with only small changes to boundary conditions and flow parameters once trained. The proposed method requires retraining with those changes.

The investigation into sample density, distribution, and noise effects further highlights the strengths and limitations of the PINN method for flow reconstruction. Higher particle density generally improved reconstruction accuracy, particularly in the pressure field. However, even when only four particles are observed in each time step, it can still capture the main feature of the pressure distribution, including the correct location of the minimum pressure. Uniformly distributed particles do not improve performance in pressure estimation compared to randomly distributed particles. The PINN model is also tested to infer the pressure field from incomplete velocity measurements, when only 2D velocities are provided for a 3D Burgers' vortex flow, demonstrating the effectiveness across diverse flow scenarios. The model also exhibits notable resilience to noise in Taylor-Green Burgers' vortex flow: the velocity fields are effectively predicted even under significant noise, and the pressure field, especially the minimum pressure value, is predicted with acceptable uncertainty. Spatial-coordinate noise can significantly degrade performance in the Lamb-Oseen vortex flow. Application to a turbulent vortex-interaction flow further suggests that the deep learning model that incorporates the physical equations can be extended to more complex flow configurations, although the training data alone do not fully represent the turbulent statistics. The pressure field reconstruction results remain reasonably accurate, with the assimilated minimum pressure close to the reference value. However, while the model reproduces the overall pressure statistics reasonably well, accurately capturing rare extreme events remains more challenging. The results indicate potential for real-world applications in flow field reconstruction, despite uncertainties arising from particle resolution, reconstruction resolution, and noise in the observation data.

ACKNOWLEDGMENTS

This work is supported by Office of Naval Research (ONR) Grant No. N00014-24-1-2013 through the Center for Naval Research and Education (CNRE) at the University of Michigan, Ann Arbor. The authors acknowledge Dr. Mehedi Hasan Bappy for sharing the numerical simulation data.

DATA AVAILABILITY

The data that support the findings of this article are not publicly available upon publication because it is not technically feasible and/or the cost of preparing, depositing, and hosting the data would be prohibitive within the terms of this research project. The data are available from the authors upon reasonable request.

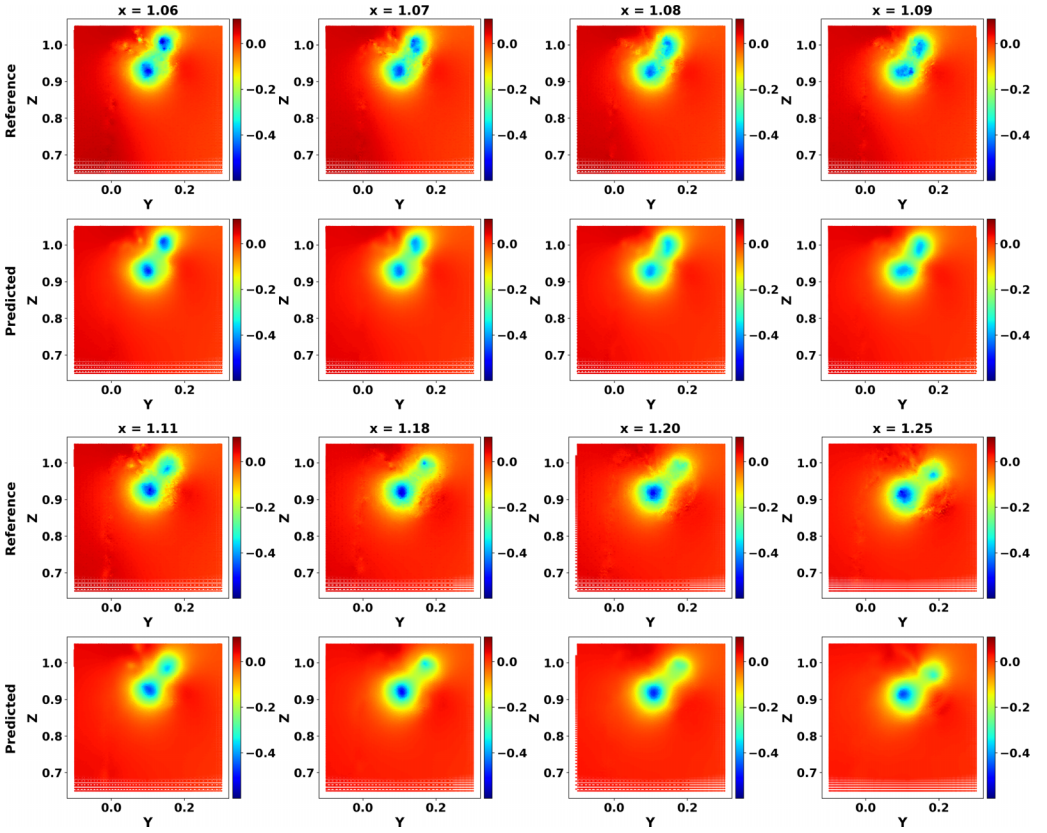

FIG. 29. Comparison of the pressure field in 2D y-z plane slice at $t^* = 2$, and multiple x locations. LES (rows 1 and 3); PINN (rows 2 and 4).

APPENDIX

More reconstruction results of the twin vortex problem are presented in this appendix. Figure 29 shows the comparison of the reference LES data and the PINN reconstruction at different x locations. Figure 30 shows the $\mathcal{L}_2$ relative errors at different time steps and x locations.

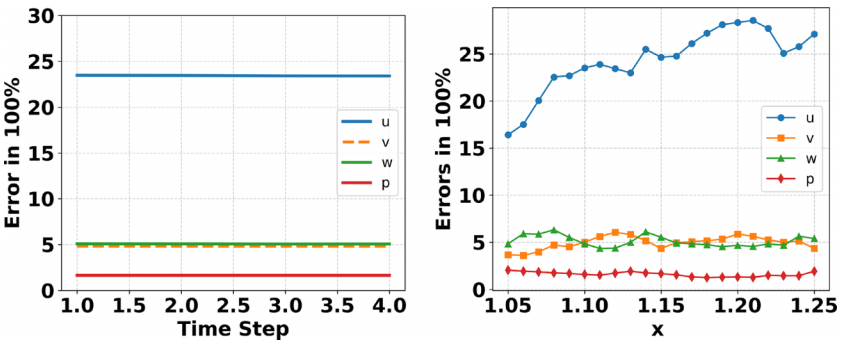

FIG. 30. LES vortex flow field reconstruction errors at different time steps and x locations.

[1] E. P. Rood, Review—Mechanisms of cavitation inception, J. Fluids Eng. **113**, 163 (1991).
[2] J. Westerweel, *Digital Particle Image Velocimetry: Theory and Application* (Delft University Press, Delft, The Netherlands, 1995).
[3] D. Knister, Experimental study of cavitation inception during vortex-vortex interaction and investigation of constrained volumetric velocimetry methods, Ph.D. thesis, University of Michigan, Ann Arbor, 2024.
[4] T. J. Leasca, T. B. Kroll, and K. Mahesh, Large-eddy simulation of the tip vortex flow in a ducted propulsor, J. Fluid Mech. **1010**, A51 (2025).
[5] B. W. van Oudheusden, PIV-based pressure measurement, Meas. Sci. Technol. **24**, 032001 (2013).
[6] Y. Murai, T. Nakada, T. Suzuki, and F. Yamamoto, Particle tracking velocimetry applied to estimate the pressure field around a Savonius turbine, Meas. Sci. Technol. **18**, 2491 (2007).
[7] X. Liu and J. Katz, Instantaneous pressure and material acceleration measurements using a four-exposure PIV system, Exp. Fluids **41**, 227 (2006).
[8] T. Suzuki, Reduced-order Kalman-filtered hybrid simulation combining particle tracking velocimetry and direct numerical simulation, J. Fluid Mech. **709**, 249 (2012).
[9] J. Zhang, S. Bhattacharya, and P. P. Vlachos, Using uncertainty to improve pressure field reconstruction from PIV/PTV flow measurements, Exp. Fluids **61**, 131 (2020).
[10] M. Wang, Q. Wang, and T. A. Zaki, Discrete adjoint of fractional-step incompressible Navier-Stokes solver in curvilinear coordinates and application to data assimilation, J. Comput. Phys. **396**, 427 (2019).
[11] D. A. Buchta, S. J. Laurence, and T. A. Zaki, Assimilation of wall-pressure measurements in high-speed flow over a cone, J. Fluid Mech. **947**, R2 (2022).
[12] A. G. Özbay, A. Hamzehloo, S. Laizet, P. Tzirakis, G. Rizos, and B. Schuller, Poisson CNN: Convolutional neural networks for the solution of the Poisson equation on a Cartesian mesh, Data-Centric Eng. **2**, e6 (2021).
[13] M. Raissi, P. Perdikaris, and G. E. Karniadakis, Physics-informed neural networks: A deep learning framework for solving forward and inverse problems involving nonlinear partial differential equations, J. Comput. Phys. **378**, 686 (2019).
[14] K. Zhou, J. Li, J. Hong, and S. J. Grauer, Stochastic particle advection velocimetry (SPAV): Theory, simulations, and proof-of-concept experiments, Meas. Sci. Technol. **34**, 065302 (2023).
[15] G. Hasanuzzaman, H. Eivazi, S. Merbold, C. Egbers, and R. Vinuesa, Enhancement of PIV measurements via physics-informed neural networks, Meas. Sci. Technol. **34**, 044002 (2023).
[16] P. C. D. Leoni, K. Agarwal, T. A. Zaki, C. Meneveau, and J. Katz, Reconstructing turbulent velocity and pressure fields from under-resolved noisy particle tracks using physics-informed neural networks, Exp. Fluids **64**, 95 (2023).
[17] X. Jin, S. Cai, H. Li, and G. E. Karniadakis, Nsfnets (Navier-Stokes flow nets): Physics-informed neural networks for the incompressible Navier-Stokes equations, J. Comput. Phys. **426**, 109951 (2021).
[18] A. Paszke, S. Gross, F. Massa, A. Lerer, J. Bradbury, G. Chanan, T. Killeen, Z. Lin, N. Gimelshein, L. Antiga, *et al.*, *PyTorch: An Imperative Style, High-Performance Deep Learning Library* (Curran Associates Inc., Red Hook, NY, 2019).
[19] L. Lu, X. Meng, Z. Mao, and G. E. Karniadakis, DeepXDE: A deep learning library for solving differential equations, SIAM Rev. **63**, 208 (2021).
[20] D. P. Kingma and J. Ba, Adam: A method for stochastic optimization, CoRR **abs/1412.6980** (2014).
[21] M. Bappy and K. Mahesh, A dynamic framework for simulating cavitation inception with large eddy simulation (unpublished).
[22] A. Madabhushi and K. Mahesh, A compressible multi-scale model to simulate cavitating flows, J. Fluid Mech. **961**, A6 (2023).
[23] S. Wang, Y. Teng, and P. Perdikaris, Understanding and mitigating gradient flow pathologies in physics-informed neural networks, SIAM J. Sci. Comput. **43**, A3055 (2021),.
[24] N. Rahaman, A. Baratin, D. Arpit, F. Draxler, M. Lin, F. Hamprecht, Y. Bengio, and A. Courville, On the spectral bias of neural networks, in *International Conference on Machine Learning* (PMLR, Long Beach, California, 2019), pp. 5301–5310.